Spatially and Temporally Resolved Delivery of Stimuli to Single Cells Using Nanocapsules and Laser Manipulation

Bingyun Sun

A dissertation submitted in partial fulfillment of the
requirements for the degree of

Doctor of Philosophy

University of Washington

2005

Program Authorized to Offer Degree: Department of Chemistry

University of Washington
Graduate School

This is to certify that I have examined this copy of a doctoral dissertation by

Bingyun Sun

and have found that it is complete and satisfactory in all respects,
and that any and all revisions required by the final
examining committee have been made.

Chair of Supervisory Committee:

Daniel T. Chiu

Reading Committee:

Daniel T. Chiu

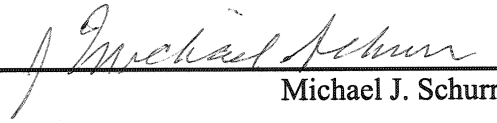

Michael J. Schurr

Younan Xia

Date: 03103105

In presenting this dissertation in partial fulfillment of the requirements for the doctoral degree at the University of Washington, I agree that the Library shall make its copies freely available for inspection. I further agree that extensive copying of the dissertation is allowable only for scholarly purposes, consistent with "fair use" as prescribed in the U.S. Copyright Law. Requests for copying or reproduction of this dissertation may be referred to Proquest Information and Learning, 300 North Zeeb Road, Ann Arbor, MI 48106-1346, to whom the author has granted "the right to reproduce and sell (a) copies of the manuscript in microform and/or (b) printed copies of the manuscript made from microform."

Signature _____

Date 03/03/05

University of Washington

Abstract

Spatially and Temporally Resolved Delivery of Stimuli to Single Cells
Using Nanocapsules and Laser Manipulation

by Bingyun Sun

Chairperson of the Supervisory Committee:
Associate Professor Daniel T. Chiu
Department of Chemistry

Cell signaling is at the core of most biological processes. The spatially and temporally resolved stimulation will help elucidate cell signaling, and lead us to a better understanding of signal transduction. We have designed and developed a technique to photolyze individual optically trapped nanocontainers for delivering spatially and temporally resolved stimuli to single cells. A submicrometer-sized nanocontainer, which encapsulates the stimuli of interest, is precisely positioned with respect to a select cell by optical trapping. Application of a single focused UV laser pulse photolyzes the trapped capsule and releases the stimuli onto a localized region of the cell. The spatial resolution of this technique is on the order of several hundreds of nanometers, while the temporal resolution lies in the sub-microsecond range. To achieve and optimize the above strategy, we have explored the synthesis/formation of a series of capsules including liposomes, inorganic and polymeric capsules with tunable size and tailored surface properties. We have created an efficient method to load the polymeric capsules with molecules of interest and developed a polyelectrolyte and silica combined coating approach to eliminate non-controllable leakage

after loading. We also initiated a novel technique to quantify the encapsulation efficiency of lipid vesicles on a single-vesicle level, which gives us a unique way to evaluate the encapsulation efficiency more meaningful than the traditional bulk anaylsis. Besides lipid vesicles, we believe this method can be broadly applied to the study of loading efficiency of other micro/nano-scale containers. We have also characterized the photo-releasing efficiency of liposomes and micro/nano capsules quantitively. Using our delivery technique, we have successfully studied carbachol-evoked calcium signaling in Chinese hamster ovary cells transfected with type-1 muscarinic acetylcholine receptors and explored the mapping of these receptors on the cell membrane.

Table of Contents

List of Figures

List of Tables

Abbreviations

CNS: central nervous system

FRET: fluorescence resonance energy transfer

SPCM: single photon counting module

PC: phosphatidylcholine

DPPC: 1,2-Dipalmitoyl-*SN*-Glycero-3-phosphacholine 16:0

PE: phosphatidylethanolamine

PG: phosphatidylglycerol

PS: phosphatidylserine

DiO-C_{18}: 3,3'-dioctadecyloxacarbocyanine perchlorate

PDADMAC: Poly(diallyldimethylammonium chloride)

PSS: poly(styrenesulfonate, sodium salt)

TEOS: tetraethylorthosilicate

Acknowledgements

This dissertation would not be possible if University of Washington, Department of Chemistry did not accept me as a graduate student five years ago. I appreciate the recognition.

In five years, every accomplishment I have achieved is under the careful advice and pamper of my supervisor Prof. Daniel T. Chiu. I really appreciate his leadership and support. To be a first graduate student of him, I learned a lot.

I would like to acknowledge the Professors I know, especially the members of my committee: Profs. J. Michael Schurr, Robert E. Synovec, Younan Xia, Sarah L. Keller, Patricia A. Campbell, and Guozhong Cao. I appreciate their kind help and support. I also would like to thank the people I got help with at University of Washington, they are Dr. Dong Qin, Greg Golden at the Center for Nanotechnology, Martin Sadilek at Mass-spec facility Lab at Department of Chemistry, and Stephanie Lara and Stephan MacFarlane at the Electron Microscopy Laboratory, Department of Pathology.

I also would like to thank all of my friends who are always so helpful, especially my labmates (Dr. David Lim, Dr. Jason Kuo, Dr. Mingyan He, Dr. Patrick Shelby, Gina Fiorini, Chris Kuyper, Robert Lorenz, Gavin Jeffries, Sarah Mutch, Peter Allen, Scott J. Edgar, Brian Morlan, Perry Schiro)

Finally I would like to thank all the organizations that had supported my projects financially, especially the two-year Nanotechnology Fellowship from the Center for Nanotechnology at the University of Washington, NIH, and McKnight Foundation.

Dedication

To my family who have supported me all the way through.

Chapter 1 Introduction

1.1 Cell signaling

Cell signaling is at the core of most biological processes such as cell division, differentiation, or regulation of specialized cellular functions. Many of these pathways have been implicated in a wide variety of diseases and key physiological functions; Figure 1-1 illustrates the calcium signaling pathways inside a cell. Cell signaling often starts from or ends at the plasma membrane.

As a heterogeneous entity, a cell responds to its environment through highly organized protein networks. Even a single type of extracellular signal acting through a single type of G-protein-linked or enzyme-linked receptor usually activates multiple parallel signaling pathways and can thereby influence multiple aspects of cell behavior-such as the shape, movement, metabolism, and gene expression of the cell. Since cell signaling is highly programmed, a spatially and temporally resolved stimulation will help to study cell signaling, and lead to a better understanding of the mechanism behind signal transduction.

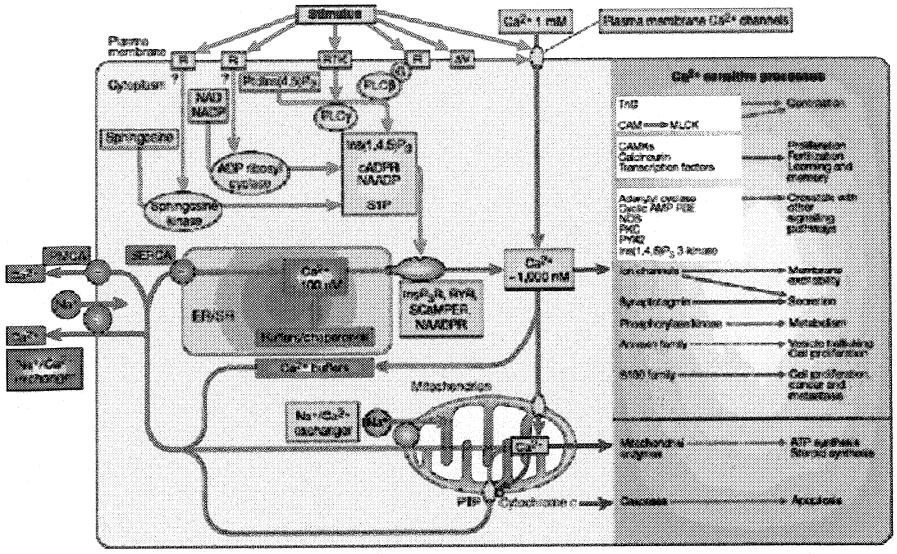

Figure 1-1 **Elements of the Ca^{2+} signalling.** Cells have an extensive signalling toolkit that can be mixed and matched to create Ca^{2+} signals of widely different properties. Ca^{2+}-mobilizing signals (blue) are generated by stimuli acting through a variety of cell-surface receptors (R), including G-protein (G)-linked receptors and receptor tyrosine kinases (RTK). The signals generated include: inositol-1,4,5-trisphosphate ($Ins(1,4,5)P_3$), generated by the hydrolysis of phosphatidylinositol-4,5-bisphosphate ($PtdIns(4,5)P_2$) by a family of phospholipase C enzymes (PLCβ, PLCγ); cyclic ADP ribose (cADPR) and nicotinic acid dinucleotide phosphate (NAADP), both generated from nicotinamide-adenine dinucleotide (NAD) and its phosphorylated derivative NADP by ADP ribosyl cyclase; and sphingosine 1-phosphate (S1P), generated from sphingosine by a sphingosine kinase. ON mechanisms (green) include plasma membrane Ca^{2+} channels, which respond to transmitters or to membrane depolarization (V), and intracellular Ca^{2+} channels — the $Ins(1,4,5)P_3$ receptor ($InsP_3R$), ryanodine receptor (RYR), NAADP receptor and sphingolipid Ca^{2+} release-mediating protein of the ER (SCaMPER). The Ca^{2+} released into the cytoplasm by these ON mechanisms activates different Ca^{2+} sensors (purple), which augment a wide range of Ca^{2+}-sensitive processes (purple), depending on cell type and context. OFF mechanisms (red) pump Ca^{2+} out of the cytoplasm: the Na^+/Ca^{2+} exchanger and the plasma membrane Ca^{2+} ATPase (PMCA) pumps Ca^{2+} out of the cell and the sarco-endoplasmic reticulum Ca^{2+} ATPase (SERCA) pumps it back into the ER/SR. (TnC, troponin C; CAM, calmodulin; MLCK, myosin light chain kinase; CAMK, Ca^{2+}/calmodulin-dependent protein kinase; cyclic AMP PDE, cyclic AMP phosphodiesterase; NOS, nitric oxide synthase; PKC, protein kinase C; PYK2, proline-rich kinase 2; PTP, permeability transition pore.). Ref 5.

1.2 Techniques available for cell-signaling studies

Many techniques are developed to study cell signaling. Most methods, however, focus on studying cellular response over a relative long time (*i.e.* minutes, hours, and even days) and require groups of cells. Although there are biophysical techniques (such as patch clamp, fluorescence resonance energy transfer (FRET), cellular imaging by confocal microscopy, evanescent wave imaging, *etc*) to monitor signaling events with good spatial and temporal resolution, the initiation of signaling is always generated by perfusion or microinjection of signaling molecules onto cell membrane or into cellular plasma, which have poor spatial and temporal resolution.

The time resolution of perfusion and injection is on the order of seconds, and the spatial resolution is on the order of micrometers, which is insufficient to study many signaling processes, such as synaptic transmission that happens in milliseconds or lipid rafts that may be submicrometers in dimensions (Figure 1-2).

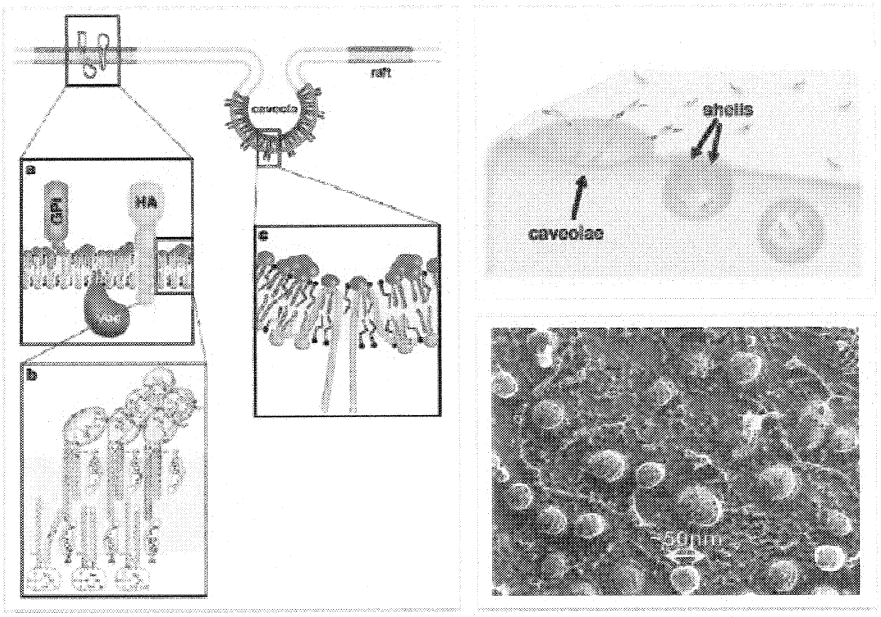

Figure 1-2. **Biological descriptions of lipid rafts.** (Left) Model for the organization of rafts and caveolae in the plasma membrane. Raft domains are shown in red and are rich in saturated lipids, cholesterol, and GPI linked proteins. Figure taken from.[1] (Right Top) Representation of "lipid shell" model.[3] Small lipid shells are building blocks of rafts and help target proteins to raft domains. Figure taken from[3] (Right bottom) Freeze fracture micrograph of caveolae on inner plasma membrane. Image from [4].

1.3 Caged molecules and two-photon excitation

Two-photon photolysis of caged molecules is a modern technique to study the dynamics of cellular responses with high spatial and temporal resolutions. Caged compounds are molecules or ions of physiological interest, and are rendered inactive by chemical modification. The modification introduces a photochemically labile bond, which on exposure to certain intensive light (such as laser) cleaves rapidly, releasing the

active compound. Two-photon excitation is a nonlinear optical process, in which the simultaneous absorption of two photons excites a molecule to a higher-energy state. This process, first studied by Göppert-Mayer in 1931,[5] now is widely used in microscopy. [6, 7] The dependence of two-photon excitation is proportional to the intensity squared, which gives this technique an intrinsic 3D resolution (Figure 1-3).

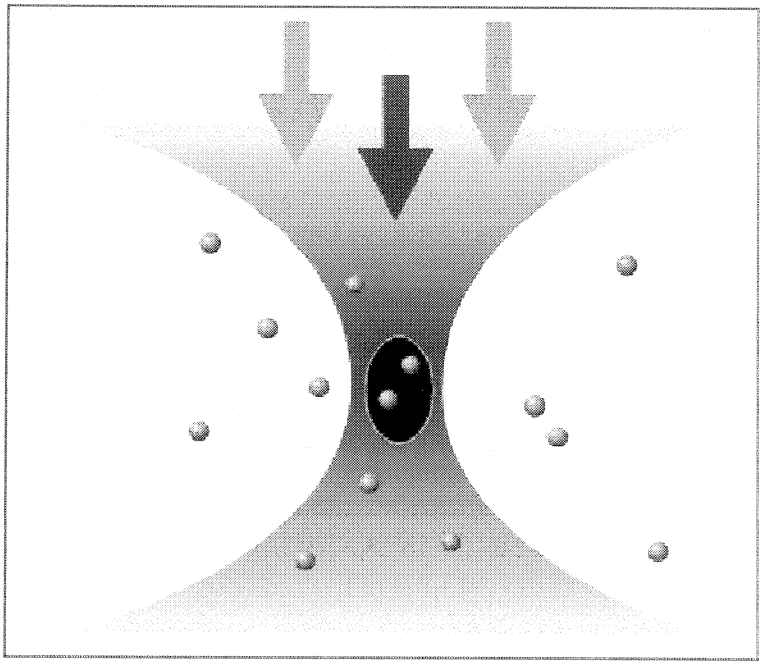

Figure 1-3. **Spatial localization of multiphoton excitation using tightly focused laser light.** The high-intensity dependence of multiphoton excitation can confine fluorescence and photochemical reactions to spatial coordinates in proximity to the focal point (region depicted as a black oval) when focusing light with high-NA optics. [2]

The special resolution of this technique is determined by the focal volume of the laser and the wavelength used. For instance, the wavelength of 1064 nm used to study biological events gives spatial resolution on the order of hundreds of nanometers. The

temporal resolution of the technique is determined by the time and efficiency of cleaving the chemical bond, and its time scale ranges from tens of microseconds to milliseconds.

Caged compounds, although widely used, suffer from several important disadvantages: (1) The design and synthesis of a suitable caged molecule is complex and time consuming, (2) The caging of large bioactive molecules, such as peptides (e.g. cytokines) and proteins, is difficult if at all possible, and (3) The uncaging of multiple stimuli simultaneously is often cumbersome.[8, 9]

1.4 Our approach — nanocontainer and laser photolysis assisted delivery

To address the limitations of using caged molecules, we have developed a new strategy by which defined packages of stimuli can be delivered to single cells with both high spatial (hundreds of nanometers) and temporal resolutions (hundreds of nanoseconds)[9]. This method uses nanocontainers to encapsulate the bioactive molecules of interest, optical trapping to manipulate individual nanocontainers with respect to a single cell, and a single 3-ns focused UV laser pulse to release the encapsulated molecules to the cell.

The use of nanocontainers, which in our case could be silica nanocapsules, hollow beads, and lipid vesicles with tailored compositions and sizes, overcomes the synthetic challenges associated with the use of caged compounds and provides a versatile platform for "caging" a broad range of molecules of interest. This approach offers new

possibilities and versatilities for studying the heterogeneous organization of cells and for unraveling the dynamics of signaling mechanisms and cellular responses.

Chapter 2 Overview of the strategy

2.1 Overview of the strategy

This dissertation focuses on the development a new strategy for delivering defined packages of stimuli to single cells with both high spatial and temporal resolutions.

The details of our strategy are illustrated in the following. Figure 2-1

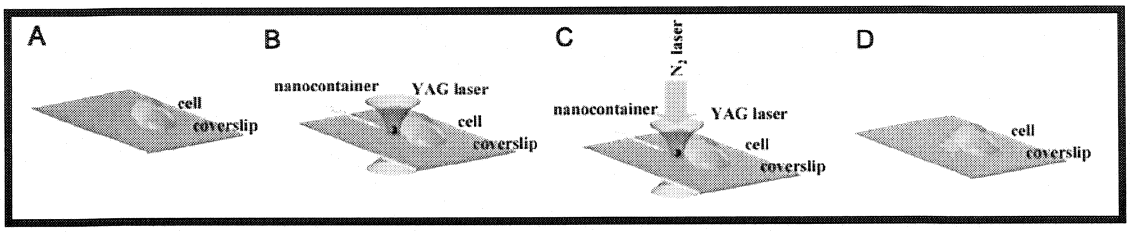

Figure 2-1. **Illustration of the experimental design.**

schematically depicts our approach. Laser optical manipulation is used to trap individual nanocontainers, encapsulating the bioactive molecules of interest with respect to a single cell. A single 3-ns pulse from a UV laser, which is aligned collinearly with the trapping laser, is used to photolyze the optically trapped nanocontainer and to release the encapsulated stimuli. The cell membrane receptors interact with the released bioactive stimuli and start the intracellular signaling responses. The spatial resolution of our technique is defined by the size of the nanocontainers; and the temporal resolution is defined by the pulsed laser duration, and the decomposing efficiency of the nanocontainer.

2.2 Setup of the optics

To fulfill the above strategy, we developed a series of optics to achieve the goal.

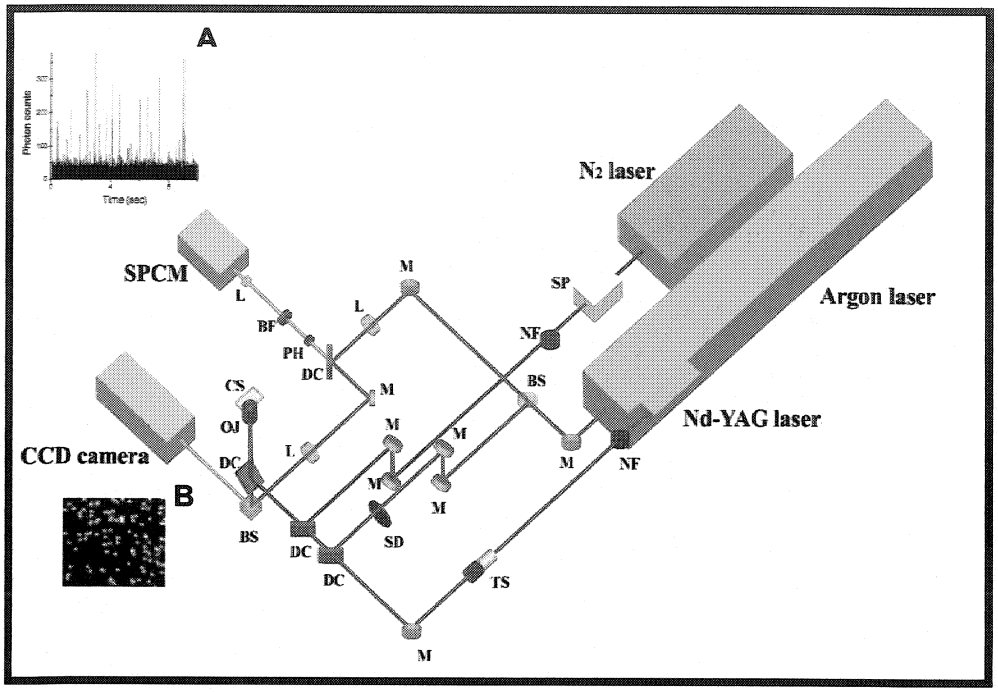

Figure 2-2. **Schematic illustration of the relative positions of the lasers**: YAG laser (red; 1064 nm; ~ 0.3 W prior to entering the N.A. 1.3 oil immersion objective), the trapped vesicle (blue), the target cell (green), and the N_2 laser (purple; 337 nm; ~ 3 μJ prior to entering the objective). Abbreviation: NF, neutrodensity filter; TS, telescope; M, mirror; SD, spin disc; DC, dichroic; SP, spatial filter; L, lens; CS, cover slip; PH, pin hole; BF, bandpass filter. Insert A, is a SPCM result of fluorescence signals emitted from 20 pM aqueous 5-carboxyrhodamine 6G solution, PBS buffer pH 7.4. The integration time of each signal line is 1 ms. Inset B, is the CCD camera image of fluorescent beads immobilized on the coverslip.

Figure 2-2 illustrates the layout of our homebuilt optics setup. Three different lasers are used: (1) an argon laser (wavelength at 488 nm) for illumination and confocal detection, (2) a Nd-YAG laser (wavelength at 1064 nm) for optical trapping and manipulation of the nanocontainers, and (3) a UV laser (wavelength at 337 nm) for photolyzing the vesicle.

All the laser beams are collimated prior to going into a microscope with 100× oil-immersion objective (1.3 numerical aperture). We use two types of detection systems to record the results, CCD camera coupled videomicroscopy is used for millisecond-timescale wide-field imaging (Figure 2-2B), and a single photon counting module (SPCM) coupled confocal microscopy is used for nanosecond-timescale point detection (Figure 2-2A).

The optical trap, also called "optical tweezers", has been around for 30 years in the physical and biological sciences for the manipulation and study of micron and submicron particles and even individual atoms.[10] In our optical setup, the Nd-YAG laser beam goes though a 1.3-numerical-aperture objective to trap and manipulate particles with sizes varying from 20 nm to 20 μm.

Confocal microscopy is another feature in our optical setup, by which we can achieve single-molecule detection sensitivity. Confocal microscopy emerged in the 1950s,[11] and quickly became an extremely useful technique in biological imaging and single-molecule studies.[12, 13] We have successfully acquired single-molecule fluorescent signals with our homebuilt confocal setup. Figure 2-2 inset A shows an example of a single-molecule trace obtained from a 20-pM carboxyrhodamine 6G in saline solution. The pulsed UV laser with 3-ns pulse duration is equipped with an external trigger that can be synchronized with the confocal SPCM detector, by which we can achieve temporal detection resolutions of 100 ns.

2.3 Consideration of the critical issues associated with this technique

To successfully implement our strategy, we must address several additional potential issues:

Nanocontainers. We must design appropriate nano-containers that are both robust and can be loaded easily withthe molecules of interest.

Encapsulation efficiency. We need to develop a technique to precisely quantify the amount of the molecules we loaded into individual containers, since we are going to use single containers to trigger cellular signaling.

Photolysis efficiency. Because the temporal resolution of our technique is determined by photolysis efficiency, we need to understand the temporal resolution of our laser-triggered release.

To address these issues, we carried out step-by-step studies and characterization, which we will discuss in detail in the following chapters (Chapter 3-7). As proof of concept, we successfully applied our technique to initiated calcium signaling in Chinese hamster ovary cells and demonstrated the potential of this method to map the receptors on the cell membrane, which is summarized in Chapter 8 & 9.

Chapter 3 Lipid vesicles as containers

3.1 Introduction of lipid

Lipids, the major component of cell membrane, are amphiphilic molecules with a hydrophilic head and hydrophobic tail groups. In aqueous solution, lipids self-assemble into double-layered structure behaving as a two-dimensional fluid. Based on different head and tail groups, lipids can be divided into different categories, and different compositions of lipids determine the properties of the bilayer membrane, such as fluidity, rigidity, and permeability.

The most abundant membrane lipids are the phospholipids, which contain a charged or polar head (including a phosphate group) attached to a glycerol backbone through an ester bond; and one or two non-polar fatty acid tail(s) dangling from the other carbons of glycerol as illustrated in Figure 3-1. Some lipid heads, such as phosphatidylcholine (PC) and phosphatidylethanolamine (PE), are neutral, while the other heads as phosphatidylglycerol (PG) and phosphatidylserine (PS) are negatively charged. The fatty acid chain could be either saturated or unsaturated, and the length could also vary from 12 carbons up to 22 carbons.

The polarity of the head group affects the surface property of lipid bilayers, for example, the repelling force between charged head groups will help to keep the lamelli of vesicles apart, so that unilamellar lipid vesicles are easier to form. The length and saturation of the tail group determines the packing of the membrane,. Lipid molecules are ordered and the movement of the lipid molecules is slow (diffusion constant is around 10^{-10} cm^2/s) [14] in the gel or solid phase. When the temperature is elevated above the

phase transition temperature of the lipid, the lipids start to behave as two-dimensional liquid, and the movements speed up (diffusion constant is around 10^{-8} cm^2/s). [14] Lipid with short length or with unsaturatedfatty acid tail has lower phase transition temperature.

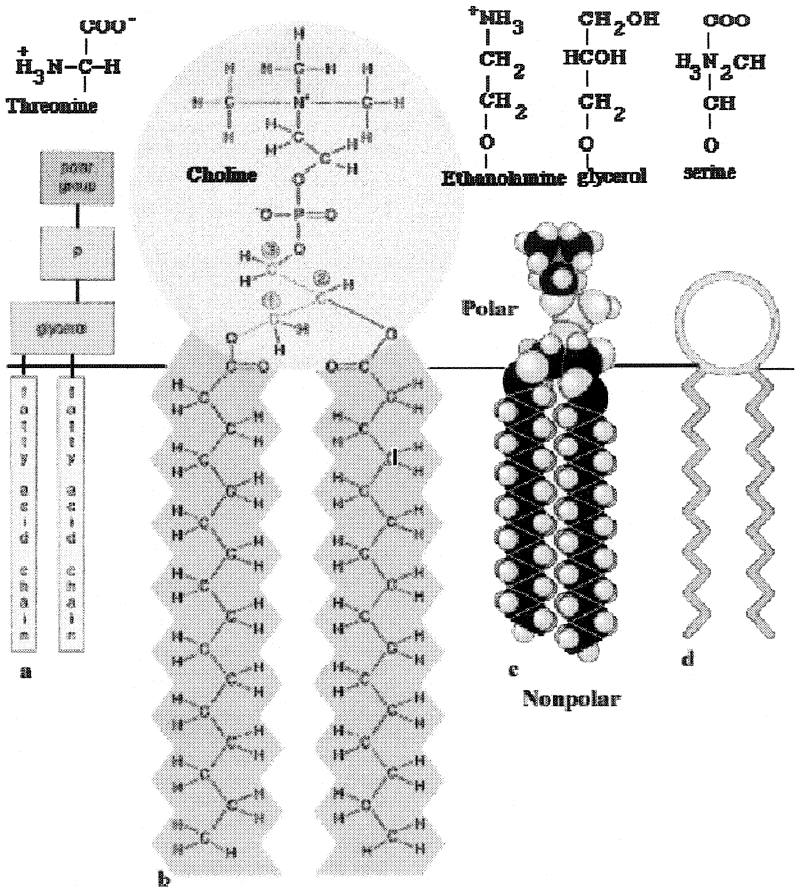

Figure 3-1. **Illustration of lipids.**

Cholesterol, ubiquitous in lipid membrane, behaves as a spacer, which can help keep the lipid molecules in order when it is in liquid phase. Cholesterol can also smooth

the sharp transition from solid to liquid at phase transition temperature; the permeability of the lipid membrane increases sharply around the phase transition temperature .

3.2 Introduction of Lipid vesicles

Lipid vesicles, also called liposomes, have been long recognized as drug carriers owing to the biocompatibility of lipid vesicles and their ability to encapsulate a wide range of molecules. As carriers for drugs, for example, lipid vesicles can be used for both sustained drug release as well as targeted drug delivery by exploiting antibody/antigen interactions. Studies have shown that drug safety and efficacy can be greatly improved and new therapies are possible when a pharmaceutical agent is encapsulated within or attached to the surface of lipid vesicles.[15-20] In addition to drug delivery, lipid vesicles have been used in diverse applications, such as model of cell membrane,[21-23] as reaction vessels,[24-30] as dye dispersants,[31, 32] and even as materials for removal of contaminated waste.[33]

Lipid vesicles have different morphology, such as size, lamellarity, and can be categorized into small vesicles (diameter between 20 ~ 100 nm), large vesicles (diameter between 100 nm ~ 1 μm), and giant vesicles (diameter between 1 ~ 100 μm) based on size; and unilamellar vesicles and multilamellar vesicles based on lamellarity. Morphology of lipid vesicle is a key factor to determine the application of lipid vesicles. In fundamental studies of membrane biophysics, for example, giant unilamellar vesicles

are often used,[21-23] whereas in drug delivery, small multilamellar vesicles are preferred.[34-36]

3.3 Formation of lipid vesicles

The formation of lipid vesicles has been studied for more than four decades. In 1965, Bangham et al. originate the hand-shaken approach [37] to form lipid vesicles and was employed to measure permeability parameters of various ions and molecules across lipid bilayers. [38] Methods based on sonication and gel filtration steps were introduced in 1969 by *Huang et al.*, [39] which provide more uniform preparations of unilamellar vesicles. We used rotary evaporation, or thin-film hydration to form giant vesicles (>1 microna), and extrusion or sonication to form small vesicles (0.5 micron).

Materials. 1,2-Dipalmitoyl-*SN*-Glycero-3-phosphacholine 16:0 (DPPC) were purchased from Avanti (Alabaster, AL). 5-carboxyrhodamine 6G, cholesteryl 1-pyrenebutyrate, 3,3'-dioctadecyloxacarbocyanine perchlorate (DiO-C_{18}) and fluo-3/AM were obtained from Molecular Probes (Eugene, OR). All the other chemicals without specification were from Sigma. All lipid vesicles in our experiments were composed of DPPC doped with a UV dye, cholesteryl 1-pyrenebutyrate (50 mol%), and/or a fluorescent dye, DiO-C_{18} (1 mol%).

Preparation of giant vesicles. The methods we use to prepare vesicles vary depending on the size of the vesicles needed. We used rotary evaporation to form lipid

vesicles having diameters greater than one micrometer, a procedure that has been described previously.[27, 40] Depending on the preparation condition and the composition of the solution and lipid, this method can give rise to vesicles with highly variable morphology. In a typical procedure, we first prepared a chloroform solution of lipids containing 9:1 mass ratio of DPPC (1,2-Dipalmitoyl-*sn*-Glycero-3-Phosphocholine) : DPPG (1,2-Dipalmitoyl-*sn*-Glycero-3-[Phospho-*rac*-(1-glycerol)] sodium salt) at concentration of 10 mg/mL and 2.5 mol % of β-py-C_{10}-HPC (1-hexadecanoyl-2-(1-pyrenedecanoyl)-*sn*-glycero-3-phosphocholine). In a 50-mL round-bottom flask, we added 50 μL of this lipid solution, and then 3 mL of aqueous loading solution (250 μM carboxyfluorescein, 0.2 M sucrose, and 50 mM borate buffer at pH 8.0) along the wall of the flask. In a rotary evaporator (Buchi, Brinkmann, NY), we evaporated away the choloform solution under reduced pressure at 50°C. We usually observed two bubbling events, one at ~ 1.5 mins after the start of evaporation due to evaporation of chloroform, and the second at ~ 2.5 mins caused by evaporation of the aqueous solution. We stopped the evaporation at the second bubbling (~ 40 mm Hg), after which an opalescent fluid was obtained with a volume of approximately 2.5 ml. We let the vesicle solution settle for ~ 30 mins, after which we passed the solution through a pre-packed 10DG size exclusion column to remove carboxyfluorescein from the extravesicular solution. We diluted this solution three fold in borate buffer (50 mM at pH 8.0) for our experiments.

Preparation of large vesicles. We used extrusion to prepare vesicles that are one hundred to several hundreds of nanometers in diameter. Briefly, giant vesicles prepared above were passed through an extruder (Avanti, Alabaster, AL) that contained a polycarbonate membrane with well-defined pore size. In most experiments, we carried out 21 passes through the membrane and used pore sizes that were either 100nm or 600nm in diameter. After vesicle formation, the molecules that were not encapsulated in the vesicles were removed by passing the vesicle solution through a size-exclusion column (Bio-Rad, Hercules, CA).

Preparation of small vesicles. Small vesicles (< 100nm in diameter) were obtained by sonicating (Ultrasonic Cleaner, Avanti, Alabaster, AL) the solution that contained giant vesicles six times for a duration of 5 min each time and at an interval of 2 min between each sonication.

3.4 Morphologies of giant lipid vesicles

We formed our vesicles using rotary evaporation, [27, 40] a method that is very sensitive to the solution (especially ionic strength of the aqueous phase), lipid composition (e.g. different lipid head groups), and the conditions (e.g. pressure and temperature) under which the vesicles are formed. Depending on the interplay of these parameters, the resulting vesicles often are very heterogeneous, both in terms of size and lamellarity.

Figure 3-2 shows both differential interference contrast (DIC) images and the corresponding fluorescence images of the vesicles we obtained using this method. To enhance the yield of giant unilamellar vesicles, we used negatively charged DPPG lipid at 10 % concentration of the DPPC lipid, because the presence of DPPG increases the electrostatic repulsion between the lamellae of the vesicles.[41, 42] We also loaded the vesicles with 200 mM sucrose, which increased the rigidity of the vesicle owing to osmotic pressure and facilitated the optical manipulation and bright-field imaging of the vesicles.[41, 42] At this concentration, the presence of sucrose inside the vesicle does not affect diffusion of the molecules after vesicle photolysis.[43]

It is evident from the images in Figure 3-2 that the morphologies of lipid vesicles are highly heterogeneous. Based on the appearance of the vesicles, we categorized them into three groups: (1) Multilamellar vesicles (MVs) that appear onion like with layered membrane throughout the vesicle and with no visible void volume (see Figure 3-2E), (2) Thick-walled vesicles (TWVs) that contain both a thick multilamellar membrane wall and a clear void volume (see Figure 3-2F), and (3) Unilamellar or Oligolamellar vesicles (OVs) that have a very thin membrane wall and which require DIC for clear visualization (see Figure 3-2G). Arrows in Figure 3-2A and 3-2B point to examples of these three groups of vesicles.

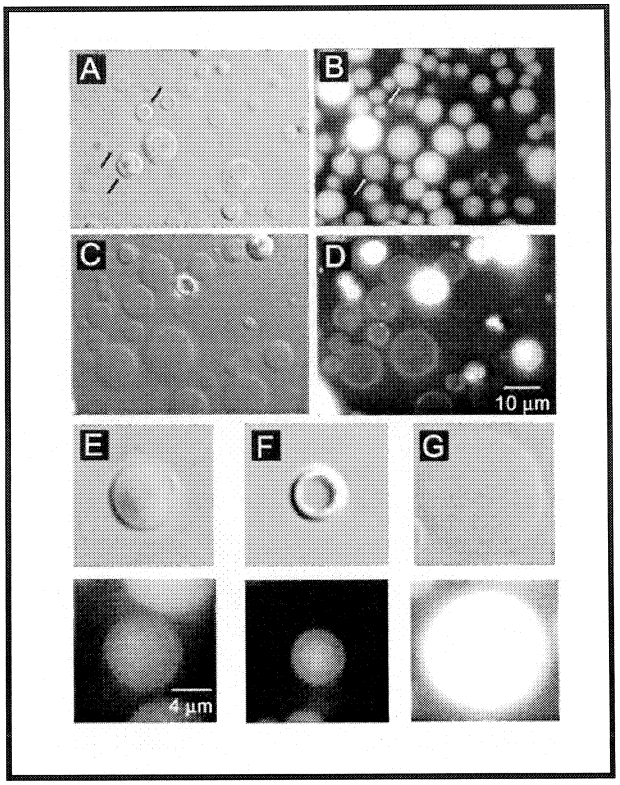

Figure 3-2. **Images of lipid vesicles.** The membrane was composed of a 9:1 mass ratio of DPPC:DPPG and 2.5 mol % of β-py-HPC. (A) and (B) are differential interference contrast (DIC) and fluorescence images of vesicles loaded with 250 µM of carboxyfluorescein, respectively. (C) and (D) are DIC and fluorescence images of the vesicles doped with 0.1 mol % of the membrane dye DiO-C_{18} (but the vesicles were not loaded with carboxyfluorescein). (E-G) are DIC and the corresponding fluorescence images of vesicles of different lamellarity that were loaded with 250 µM of carboxyfluorescein. (E) multilamellar vesicles (MVs), (F) thick-walled vesicles (TWVs), and (G) oligo-lamellar vesicles (OVs).

To further visualize the lipid membranes of these different vesicles, we doped the membrane with the fluorescent membrane dye, DiO-C_{18}, and imaged these vesicles both under DIC and fluorescence (Figure 3-2C and 3-2D). With a thin membrane layer and a large void volume, OVs exhibit a well defined fluorescent membrane layer and non-

fluorescent interior. In contrast, the presence of multiple layers of DiO-C_{18} stained membranes made the MVs and TWVs both highly fluorescent and obscured any void volumes that might be present in these vesicles (Figure 3-2D). The size of vesicles ranged from submicrometers to tens of micrometers. Below ~ 1-2 μm in diameter, however, it became difficult for us to distinguish clearly among these three groups of vesicles.

Chapter 4 Encapsulation of Lipid Vesicles

4.1 Importance

Regardless of the application of lipid vesicles as containers as we mentioned in previous chapters, an important parameter in using vesicles is the efficiency with which they can encapsulate the molecules of interest. This encapsulation efficiency (EE) is sensitive to a number of factors associated with vesicles, such as the physical properties of the membrane surface, including charge, hydrophobicity, and rigidity,[44] the characteristics of the chemicals to be encapsulated,[45] and the method used to prepare the vesicles.[46] A method capable of quantifying the encapsulation efficiency of vesicles, with single-vesicle resolution as a function of vesicle morphology, will benefit a range of research areas that use vesicles.

Differences in the encapsulation efficiencies among vesicles as a function of morphology have been reported,[35, 36, 45, 47] but these experiments were based on bulk analysis and represented the average EE of a given preparation. In addition, such bulk analysis suffers from the inability to distinguish: (1) molecules that are encapsulated within vesicles from extravesicular molecules that arise either from leakage or from the original preparation,[46] and (2) molecules present in the vesicles that can be released from those that are absorbed onto the surface of the vesicle membrane.[46]

Because vesicle morphologies can be highly heterogeneous within a given preparation, a method capable of measuring the EE of single vesicles is required to study such heterogeneities.[45-47] Given the recent interests in using individual vesicles as micro and nano scale reactors,[24-30] methods for studying the EE at the single-vesicle level are

becoming more pertinent. There is no method currently, however, for accurately measuring the efficiency of encapsulation and release from individual vesicles or other micro and nano scale containers.

To overcome the drawbacks of bulk analysis and to address the need to measure the EE of individual vesicles, this paper describes a method for monitoring the release from a single vesicle and to determine the EE of the vesicle. This method is based on the optical trapping and laser photolysis of a select vesicle and the subsequent detection of the small amounts of releasates from the photolyzed vesicle using single-molecule confocal fluorescence detection. By monitoring the transit times and the number of released molecules, we can accurately deduce the concentration of the molecules present in the vesicle. Because confocal detection records the background fluorescence prior to photolysis, our measurements distinguish easily the molecules that are actually released from the vesicle from those that are present in the extravesicular solution prior to release. This method also distinguishes released molecules from those that are absorbed onto the vesicle membrane and are thus unavailable for release into solution.

4.2 Optical setup

Our optical setup has been described previously.[48, 49] Briefly, we used three lasers to conduct our experiments (see Figure 4-1): an Ar^+ laser (Stabilite 2017, Spectra-Physics, CA; wavelength at 488 nm) for epi-illumination and confocal fluorescence detection, an Nd-YAG laser (J20-BL10-1064Q, Spectra-Physics, CA; wavelength at 1064

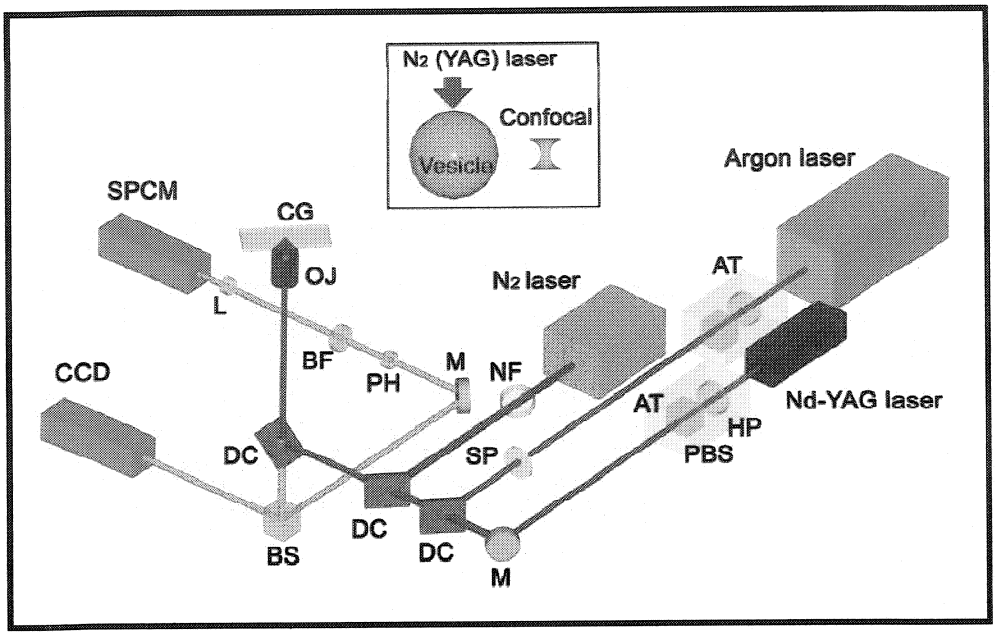

Figure 4-1. **Schematics of the instrumentation**: AT, attenuator (HP, half-wave plate; PBS, polarizing beam splitter); M, mirror; DC, dichroic beam splitter; SP, spinning plate; BS, beam splitter; OJ, objective; CG, cover glass; PH, pin hole; BF, bandpass filter; L, lens; SPCM, single photon counting module. The inset shows the relative placement of the vesicle with respect to the confocal detection volume and the focus of the N_2 laser; the YAG laser was aligned co-linearly with the N_2 laser.

nm) for optical trapping, and a pulsed N_2 laser (VSL-337ND-S, Laser Science Inc., MA; wavelength at 337 nm with pulse duration of ~ 3 ns) for photolyzing individual vesicles. We varied the power of the N_2 laser with neutral density filters (Thorlabs, Inc., Newton, NJ) and the power of the Ar^+ and YAG laser with half-wave plates and polarizing beam splitters. The outputs of the three lasers were aligned co-linearly and directed into a100 × oil immersion objective (N.A. = 1.3) via a series of dichroics and mirrors.

The fluorescence photons emitted from the sample were collected by the same objective and directed either onto a CCD camera (Cohu Inc., Poway, CA) for wide-field

imaging, or onto a single-photon counting module (SPCM) (Perkin-Elmer, Wellesley, MA) for point detection. Signal from the SPCM was collected by a multichannel scalar card (MCS-PCI from Ortec, Perkin Elmer, CA), which was also used to trigger the firing of the N_2 laser pulse to synchronize data collection with laser photolysis. Images were either recorded by a high definition VCR (VHS HR-VP78U, JVC Americas Corp., Cypress, CA) and then digitized with a DT3120 frame grabber card (Data Translation Inc., Marlboro, MA) and Global-lab image/2 software, or digitized directly by an Osprey-210 video capture card (ViewCast Corp., Dallas, TX) with VirtualDub software. The powers of the Ar^+ laser, YAG laser, and N_2 laser prior to the objective were ~ 0.5 mW, ~ 0.2 W and ~ 1 μJ, respectively.

4.3 Photolysis and release from single lipid vesicles

To trigger the release from a single vesicle, we either trapped the vesicle in solution with the YAG laser and photolyzed the vesicle in solution with a single 3-ns pulse from the N_2 laser or we placed the vesicle first on the surface of the coverslip followed by single-pulse photolysis. In either case, the YAG and N_2 laser were aligned co-linearly so their respective foci overlapped (Figure 4-1). To measure the release from the photolyzed probe volume was ~ 0.5 μm in diameter (at the beam waist) and ~ 1 μm in height.[30]

For efficient photolysis of vesicles with low pulse energy (~ 1 μJ), we doped the membrane with 1-hexadecanoyl-2-(1-pyrenedecanoyl)-*sn*-glycero-3-phosphocholine (β-

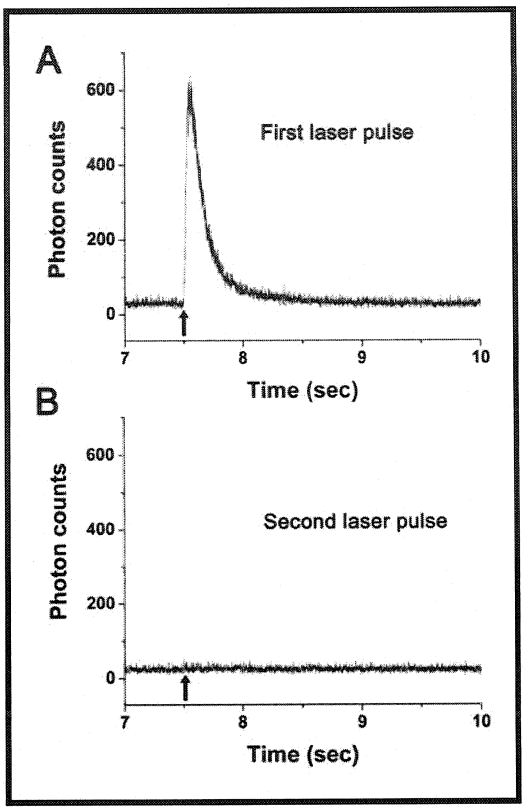

Figure 4-2. **Single-pulse photolysis of a vesicle** (9:1 mass ratio of DPPC:DPPG and 2.5 mol% β-py-HPC) containing 250 μM of carboxyfluorescein. (A) A single 3-ns laser pulse at 337 nm caused the release of carboxyfluorecein from the vesicle, which was monitored by confocal detection. (B) Application of a second laser pulse caused no detectable release, indicating the content of the vesicle was released completely after the first laser pulse. The arrows mark the firing of the N_2-laser pulse. The energy of the pulse prior to the objective was ~ 1 μJ.

py-C_{10}-HPC) (at 2.5 mol%), which has strong absorption at the N_2 laser wavelength of 337 nm.[9, 30] With this UV sensitizer, we could reproducibly photolyze individual vesicles using a single UV laser pulse, which caused the release of all the molecules encapsulated in the vesicle. Figure 4-2 shows this complete release after single-pulse photolysis. After the first pulse, confocal detection recorded the arrival and passage of

the released dye molecules (Figure 4-2A), but no additional release could be detected with application of more UV laser pulses (Figure 4-2B).

4.4 Confocal detection

The small volume of individual vesicles (femtoliters) translates into small amounts of encapsulated and released molecules. To detect these molecules requires a detection method that is highly sensitive and offers high spatial resolution. We employed confocal detection to monitor the arrival and passage of the fluorescent molecules that were released from the vesicle, owing to the high sensitivity of confocal detection and its ability to detect even a single molecule with high signal-to-noise ratio. To correlate the number of photons that we detected with the number of molecules that were present in solution, we monitored the increase in the number of photon counts we observed as we increased the concentration of carboxyfluorescein in solution. For most of the experiments described here, the concentration of carboxyfluorescein in solution was in the nanomolar range, in which case the correlation between the number of observed photons and the concentration of molecules was perfectly linear. At lower concentrations in the picomolar range, there was still good linear correlation, although not nearly as good as in the nanomolar range.

Figure 4-3(A-D) shows typical photon traces at 10, 50, 100, and 500 pM, respectively. Each photon spike corresponds to the entrance and exit of a fluorescent molecule into and out of the confocal detection volume. As the concentration of the

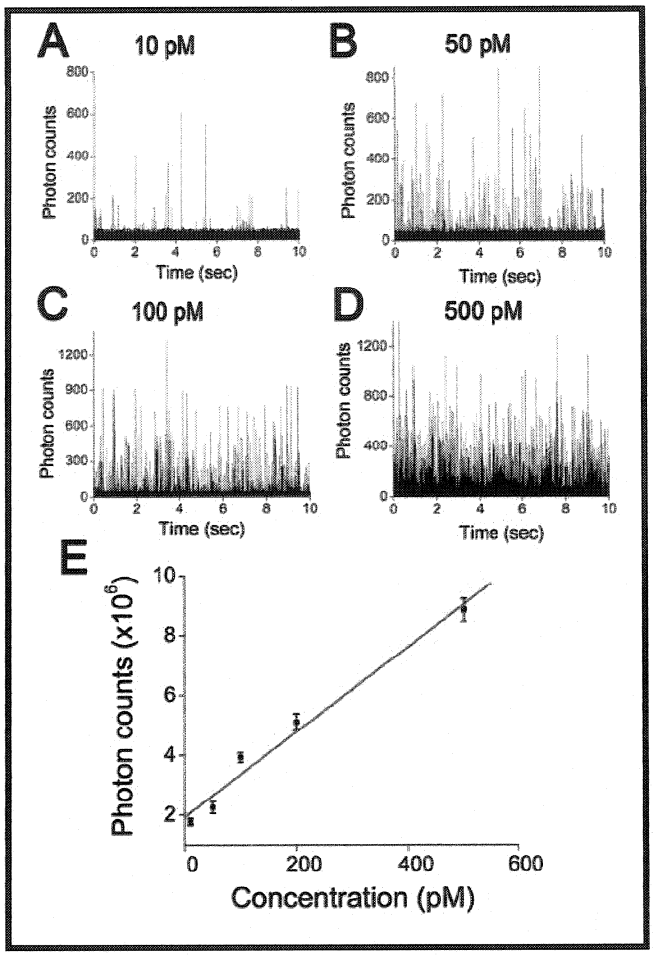

Figure 4-3. **Correlation of the concentration of carboxyfluorescein (in the picomolar range) with the number of photons collected by confocal detection.** (A-D) are representative signals obtained by confocal detection from carboxyfluorescein at different concentrations in 50 mM borate buffer. (E) Plot of total collected photon counts as a function of the concentration of carboxyfluorescein.

molecules increased, the frequency of detecting a single molecule increased, which led to a higher frequency of detected photon spikes. Figure 4-3E plots as a function of concentration the number of total detected photons in the photon trace, which was obtained by summing the number of photons in each photon spike after subtracting away

the background noise. This plot indicates that even at very low concentrations of picomolars, confocal detection can still be used reliably to determine the concentration of fluorescent molecules in solution.

4.5 Determination of encapsulation efficiency of single vesicles

To determine the encapsulation efficiency of single vesicles, we first measured the amount of molecules released from the vesicle after single-pulse photolysis using confocal detection. By placing the confocal probe volume a few micrometers outside the vesicle and by recording the transit times and the number of the released molecules that crossed the detection volume upon laser photolysis, we could calculate the total number of molecules released from the vesicle. Figure 4-4A shows a representative measurement; the inset shows the relative position of the confocal laser probe volume and the YAG (and N_2 that overlapped with the YAG focus) trapping laser where the center of the vesicle was located. The arrow in the time trace marks the firing of the N_2 laser pulse.

To calculate the number of molecules released from the vesicle, we used the following equation that describes three-dimensional diffusion from a point source:

$$C(r,t) = \frac{N}{(4\pi Dt)^{3/2}} e^{-r^2/4Dt} \qquad (1)$$

where $C(r, t)$ is the concentration of molecules we measured at position r (the distance between the center of the vesicle and the confocal detection volume) and at time t, N is

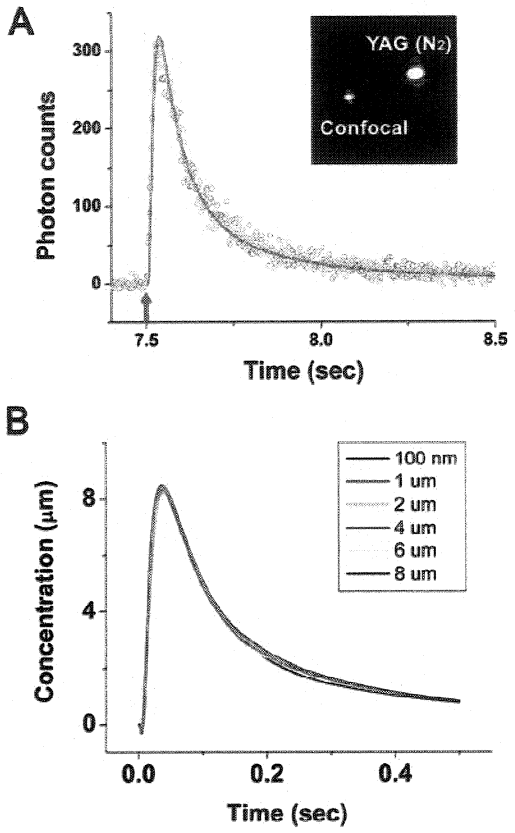

Figure 4-4. **Determination of encapsulation efficiency of single vesicles.** (A) Experimental data (open circles) and curve fit (red line) of the time trace that arose from the arrival and passage of the released carboxyfluorecein molecules across the confocal probe volume. The inset is a CCD image of the back reflection at the coverslip of the Ar^+ and YAG laser foci, which illustrates the relative placements of the three lasers; the N_2 laser focus overlapped with the YAG focus. Arrow marks the firing of the N_2 laser. The powers of the Ar^+ laser, YAG laser, and N_2 laser prior to the objective were ~ 0.5 mW, ~ 0.2 W and ~ 1 μJ, respectively. (B) Simulated time traces showing release from vesicles of different diameters (100nm, 1 μm, 2 μm, 4 μm, 6 μm, 8 μm) as monitored by confocal detection. The confocal probe volume was placed 10 μm away from the center of the vesicles in all cases. Each vesicle contained 7.8×10^7 carboxyfluorescein molecules, which corresponded to 250 μM of carboxyfluorescein contained in a 10 μm vesicle. The simulation was carried out in FEMLAB.

the number of molecules released from the vesicle, and D is the diffusion coefficient of the molecule. We can fit our measured time trace to this equation (Figure 5A) to find out N. Knowing N and the size of the vesicle, which we can measure from our microscope image, we can calculate the concentration of molecules present in the vesicle prior to release. The encapsulation efficiency is easily obtained by dividing this concentration inside the vesicle with the concentration of the molecules in the original loading solution.

(A) FEMLAB simulation: One potential issue is whether Equation 1 describes our experiment accurately, because our vesicle is not a point source. Intuitively, equation 1 should still be valid provided the confocal detection volume is "sufficiently far" from the vesicle. To address this issue and to determine whether our detection volume was "sufficiently far" from the vesicle, we carried out a detailed simulation study using FEMLAB (Mathworks Inc., Natick, MA).

In this simulation, we placed a fixed number of molecules into the vesicle, which corresponded to a concentration of 250 μM within a 10 μm diameter vesicle. We varied the size of the vesicle from 100 nm to 8 μm, while maintaining the same separation distance of 10 μm from the center of the vesicle to the confocal detection volume. Similar to our experiment, we could record in our simulation the arrival and passage of the released molecules through the confocal detection volume. In the following, we will first describe the parameters of our simulation, then a discussion of our results.

After photolysis of the vesicle, the time-dependent diffusion process in three-dimensional spherical cooridinates is described by:[50]

$$\frac{\partial}{\partial t}c = D\frac{1}{r^2}\frac{\partial}{\partial r}\left(r^2\frac{\partial c}{\partial r}\right) \qquad (2)$$

where c is the transient concentration of the molecules at time t and at position r from the center of the vesicle, and D is the diffusion coefficient (4.25×10^{-6} cm^2s^{-1}).[51] Equation 2 was solved subject to the following initial condition (IC) and boundary condition (BC) for a vesicle of radius r_v. Prior to photolysis, the concentration within the vesicle is C_{in} and is zero everywhere else:

$$\text{IC:} \quad \begin{aligned} C(r \le r_v, t = 0) &= C_{in} \\ C(r \ge r_v, t = 0) &= 0 \end{aligned}$$

After photolysis, the system was subjected to the following no-flux boundary condition:

$$\text{BC:} \quad \frac{\partial c}{\partial r}(r = \infty, t > 0) = 0$$

To obtain a numerical solution, we set r_∞ to be r_{max} = 1 mm, which is ~ 1000 × the radius of the vesicle (r_v).

Figure 4-4B shows the result of the simulation, which are simulated time traces for vesicles with diameter of 100 nm, 1 μm, 2 μm, 4 μm, 6 μm, and 8 μm, respectively; the separation distance of 10 μm between the center of the vesicle and the confocal detection volume remained constant. At this separation distance of 10 μm, the vesicle with diameter of 100 nm approximates a point source while the one with diameter of 8 μm is far from a point source. Yet, the simulated traces showed remarkably little difference between these two cases and for vesicles with diameters that ranged between

these two values. Intuitively, this result indicates the concentration profiles that arise from diffusion from a point source (vesicle of 100 nm) and from an 8-μm vesicle appear approximately the same at 10-μm away where confoal detection occurs, because diffusion is very efficient in smoothing out the differences. From this study, we conclude we can reliably calculate from our measured time trace based on Equation 1, the number of molecules contained within a vesicle.

(B) Data fitting: To fit our measured time trace and to obtain N, the number of molecules released from the vesicle, we further modified Equation 1:

$$Np(r,t) = k \times \frac{C_{in} \times V_{ves}}{(4\pi Dt)^{3/2}} e^{-r^2/4Dt} \qquad (3)$$

where Np is the number of photons detected in the confocal probe volume, V_{ves} is the volume of the vesicle, C_{in} is the initial concentration of the molecules in the vesicle, and k (9.65×10^6 m^3/mol for carboxyfluorescein) is the ratio between the number of photons detected and the concentration of the molecules in solution. We obtained k by calibrating our confocal detection with different known concentrations of molecules present in solution. Data fitting was carried out using the Origin software (OriginLab Corporation, Northampton, MA).

Figure 4-4A shows a typical data fit, where the open circles are measured data and the red trace is the fit. Once we have obtained C_{in}, we can calculate the encapsulation efficiency (EE) (in percentage) for each vesicle:

$$\text{EE (\%)} = C_{in} / C_{orig} \times 100\ \%$$

where C_{orig} is the concentration of the molecules in the original loading solution in which the vesicles were formed.

4.6 Characterization of encapsulation efficiency of individual vesicles

We used the method described above to determine the encapsulation efficiency of the giant vesicles we prepared (Figure 3-2). Giant lipid vesicles are widely used as models in the study of membrane properties[21, 23, 52-55] and as biomimetic reaction containers.[24-30] In addition, giant lipid vesicles are often the starting material for the preparation of small vesicles (e.g. by extrusion), which are commonly used in drug delivery,[15-20] food processes,[56] and many other applications.[31, 32] It is, therefore, important to understand how encapsulation efficiency may vary among individual giant lipid vesicles.

Figure 4-5 summarizes the encapsulation efficiency (EE) we determined for individual vesicles; we used 250 μM of carboxyfluorescein in our loading solution. Here we studied oligolamellar vesicles (OVs) (empty circles) and multilamellar vesicles (MVs) (solid circles). There is a wide range of EEs among OVs, ranging from as low as 0.76 % to as high as 68 %; the average EE was 36.3 ± 18.9 % (N = 17). The MVs showed a narrower distribution, ranging from 6 % to 31 % with an average of 17.5 ± 8.9 % (N = 16). Overall, OVs showed a higher EE than MVs, because there is more void volume in OVs to accommodate the encapsulated molecules. The wide range of EE for OVs may be caused by leakage during the vesicle purification procedure, owing to the thin membrane layer.

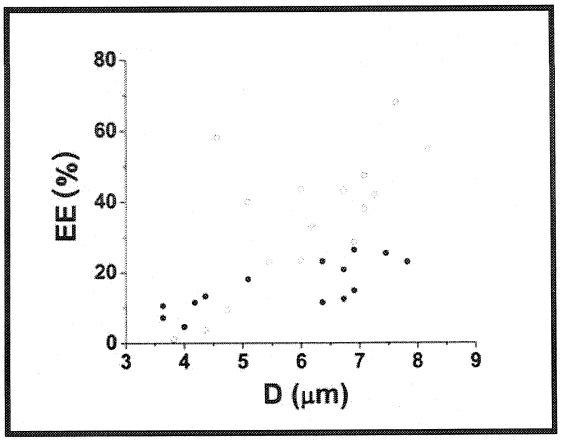

Figure 4-5. **Plot showing the encapsulation efficiency of single vesicles as a function of size and lamellarity**; (•) denotes multilamellar vesicles (MVs), and (o) denotes the oligo-lamellar vesicles (OVs). All vesicles were composed of 9:1 mass ratio of DPPC:DPPG and 2.5 mol% of β-py-HPC, and contained 250 μM carboxyfluorescein.

Our result indicates that on average OVs have a higher EE than MVs, which is consistent with reports of previous bulk analysis, although some of these bulk studies have reported much larger differences in EE (e.g. OVs has > 6× the EE than MVs [35, 36, 45]) than we have observed. These differences can be caused by differences in vesicle preparation, but they also arise from the difficulty in arriving at a consistent definition to characterize encapsulation in bulk assays. Two common definitions are: (1) Bulk Encapsulation Yield (BEY)[47] (also referred to as encapsulation efficiency,[46, 57] encapsulation capacity[36, 58, 59]), which is calculated by dividing the total amount of solutes in vesicles by the total amount of solute in the original loading solution at a particular lipid concentration (i.e. Σ solute in vesicle / Σ solute in original solution).[56-58] BEY is thus highly dependent on the number of vesicles present in solution, because even if each vesicle encapsulates a small amount of solutes, the BEY can be high if there are many

vesicles. The single-vesicle analysis described here overcomes this issue. (2) Bulk Encapsulation Efficiency (BEE)[35, 44, 45, 47, 60] (also referred to as molar fraction[36]), which is calculated by dividing the total amount of solutes in vesicles by the total amount of lipid present in solution (i.e. $\sum$ solute in vesicle / $\sum$ lipid in solution). This definition aims to take into account the number of vesicles in solution, but in so doing it does not take into account the concentration of solutes in the original loading solution and does not describe how efficiently vesicles encapsulate solutes during the loading process. As numerous groups have pointed out,[45, 57, 61] BEY will increase by increasing the amount of lipids added to form vesicles while BEE will actually decrease.

These difficulties with defining a meaningful EE originate from the inability of bulk assays to measure EE with single-vesicle resolution. We believe our definition of EE, which is made possible by our ability to measure directly the contents of and release from individual vesicles, circumvents the problems associated with bulk assays and offers a more precise method to study the encapsulation efficiency of lipid vesicles or other micro and nano scale containers.

4.7 Conclusion

We have been able to develop different approach to form lipid vesicles with variety of morphologies as drug carrier and containers to fulfill other applications, and we have innovated a new technique to characterize individual encapsulation efficiency of individual lipid vesicles more precise and accurate than any other current approaches

available, which will rise the possibility to study the property of lipid vesicles more extensively, and can open new avenue for the application of lipid vesicles.

The main drawback of our method is its inherent low throughput, because vesicles have to be analyzed one at a time. The cause of this drawback is also the source of the advantages of this approach. We can define an encapsulation efficiency more meaningful than traditional definitions based on bulk studies, because we can achieve single-vesicle resolution in our analysis. We measure only the molecules that are released from the vesicles, and can distinguish molecules that are present in solution prior to release or molecules that cannot be released because they are absorbed onto the surface of the vesicle. In addition to lipid vesicles, this method can be applied equally well to other micro or nano scale containers. To increase the throughput of this technique, schemes for the parallelized photolysis of vesicles and the subsequent detection of releasates would have to be developed. Recent advances in the formation of large arrays (hundreds) of optical traps and the diffractive generation of large arrays of laser foci [62] may find use in the parallelization of these single-vesicle measurements.

Chapter 5 Nanoparticles as drug carriers

5.1 Introduction of nanoparticles

Capsules of both inorganic (metal, metal oxide, and ceramic) and organic (polymeric) materials have been extensively studied and reviewed in the literature.[63-65] We focused on the synthesis and loading of silica and polystyrene-acrylic based nanocapsules with small molecules. The nanocapsules are used for delivering defined packages of stimuli to single cells with both high spatial and temporal resolutions as illustrated in Figure 2-1. To introduce molecules into the capsules, we characterized two approaches. The first approach is based on a base-swell process in which the shell of the capsule is swelled so small molecules can diffuse into the interior of the capsule and be trapped inside once the capsules are de-swelled. The second approach is based on a dry-swell-dry process in which the solution containing the molecules of interest and the nanocapsules is physically dried to promote more molecules to enter into the interior of the capsule.

We characterized both methods by monitoring the content of and the release from individual capsules with confocal microscopy and wide-field imaging. At the meantime, we also tested the leakage encapsulated into the hollow latex beads, and developed a polyelectrolyte/silica coating to prevent the potential leakage.

5.2 Synthesis of inorganic capsules

Synthesis of silver nanoparticles. A polyol process[66-68] was used to synthesize silver nanoparticles with different sizes. Silver nitrate, the precursor, was reduced by

ethylene glycol (EG), which also served as the solvent. Poly(vinylpyrrolidone) (PVP, Mw ≈ 10 000) was used as the protecting agent to prevent the aggregation of silver particles. In a typical experiment, 2g of PVP was added slowly into 15 ml of an EG solution of 80 mg $AgNO_3$ under continuous magnetic stirring. This reaction mixture was heated to 120 °C at a rate of ~ 1°C per min, after which the reaction was allowed to proceed for 1 hr at 120 °C. The reaction mixture was allowed to cool down to room temperature and acetone (> 200 ml) was then added to dilute this reaction mixture. The silver colloidal particles formed were separated from this solution by centrifugation, and were then re-dispersed in ethanol.

We characterized the silver nanoparticles with transmission electron micrographs (TEM) were acquired on a JEM-1200EX II electron microscope (JEOL) with an accelerating voltage of 80 kV. The sample was dispersed by alcohol on a carbon-coated copper grid. Figure 5-1 is transmission electron microscopy (TEM) images of the resultant silver colloids, in which the average sizes were tuned from 25 nm to 200 nm.

We used the polyol process[66-68] to synthesize silver nanoparticles of different sizes, in which the precursor, silver nitrate, was reduced by ethylene glycol (EG) in the presence of poly(vinylpyrrolidone) (PVP) to form dispersed colloidal silver. PVP was added to the reaction mixture to prevent the aggregation of silver particles. Based on previous reports, PVP can also reduce $AgNO_3$.[66, 67, 69] The sizes of the resultant silver particles can be tuned by varying the ratios of $AgNO_3$, EG, and PVP as well as the temperature in which the reaction is carried out.[66, 67]

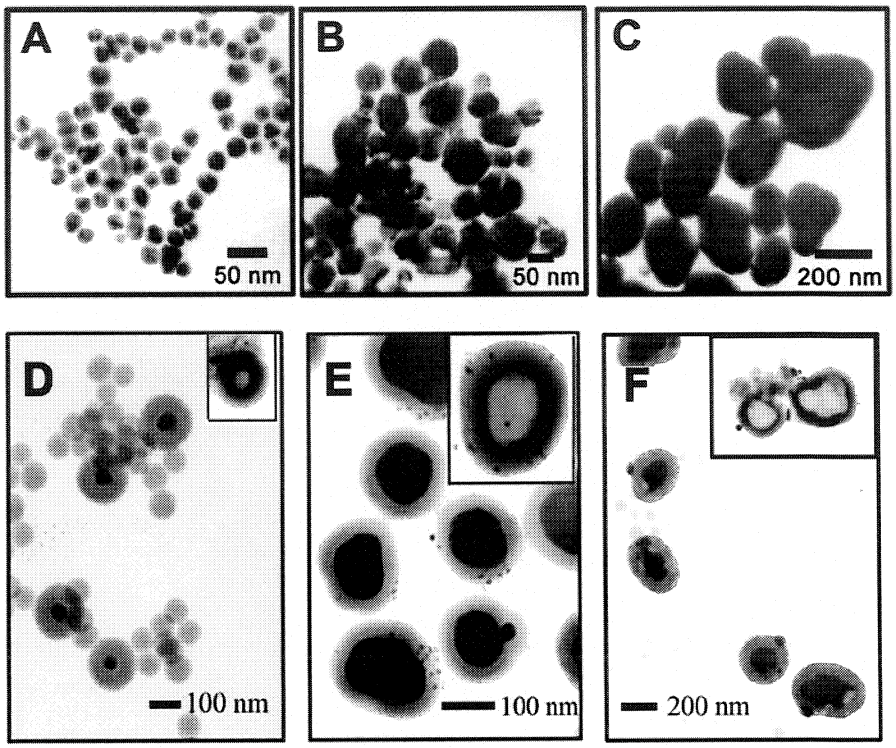

Figure 5-1. TEM images of the nanocapsules. (A-C) TEM images of silver colloids formed under the following experimental conditions: (A) Sample 1: 0.08 g $AgNO_3$, 2 g PVP, and 15 ml EG, at 120 °C; (B) Sample 2: 1.0 g $AgNO_3$, 2 g PVP, and 15 ml EG, at 120 °C; and (C) Sample 3: 0.21 g $AgNO_3$, 0.21 g PVP, and 11 ml EG, at 160 °C. **(D-F)** TEM images of silica coated silver colloids ; the insets show the resultant silica nanocapsules

Table 5-1 lists the different conditions under which silver nanoparticles shown in Figure 5-1(A-C) were prepared. Increased temperature and ratio of $AgNO_3$ to PVP led to the formation of larger silver particles;[66, 70] however, the control over the homogeneity, shape, and crystallinity of the particles was diminished, since less PVP was used. EG and PVP assisted reduction of $AgNO_3$ is one of the best methods to form colloidal silver with

a narrow size distribution,[66] although the formation of large particles (>50 nm) achieved by decreasing the PVP to $AgNO_3$ ratio will broaden this size range. A number of methods exist for the formation of other metal colloidal particles with good homogeneity in size, such as gold nanoparticles that have a less than 10% variation in diameter,[71] but it is in general difficult with these methods to form large particles (> 100 nm) while maintaining this narrow distribution in sizes.

Table 5-1. The average size of silver particles formed as a function of the concentration of $AgNO_3$, PVP, EG, and the reaction temperature. S. D.: standard deviation.

Sample number	Average size of silver particles (nm)	S.D. (N=25)	$AgNO_3$ (g)	PVP (g)	EG (ml)	Reaction temperature (°C)
1	22	3.2 (14.5%)	0.08	2	15	120
2	65	15 (23.1%)	1.0	2	15	120
3	1.8×10^2	50 (27.8%)	0.21	0.21	11	160

Formation of silica nanocapsules: To form silica nanocapsules, the Stöber method [72-74] was used to coat the silver colloids with amorphous silica. Approximately 2.4 mg of the silver colloids were dispersed into a mixture of 20 ml of 2-propanol and 4 ml of de-ionized (DI) water, after which 1 ml of 30% ammonia solution and 0.01 ml of tetraethylorthosilicate (TEOS) were added consecutively to this solution. After the reaction had proceeded for 30 mins, the final mixture was centrifuged at 8000 rpm to isolate the silica-coated silver nanoparticles, which were then re-dispersed in DI water.

Silica nanocapsules were formed from the silica-coated silver nanoparticles by dissolving the silver core overnight in a solution of ammonia at pH ~10.

Figure 5-1(D-F) shows the results of this process, which are TEM images showing silica coated silver nanoparticles of different sizes. The thickness of the silica shell can be tuned by adjusting the amount of NH_4OH and the concentration of TEOS present in the reaction mixture, as well as by controlling the reaction time.[72, 73] More NH_4OH or TEOS or longer reaction time leads to a thicker silica coating on the silver particles (heterogeneous nucleation process) as well as the formation of pure silica particles (homogeneous process) (Figure 5-1(D-F)). By increasing the concentration of silver colloids or by decreasing the concentration of TEOS, the homogeneous process can be essentially eliminated (Figure 5-1E).

To form nanocapsules, the silver core was etched away in an ammonia solution, thereby leaving behind a silica shell. The insets in Figure 5-1(D-F) show examples of such nanocapsules. Because the silica shell was formed in a basic environment in which silica can also experience slow hydrolysis, a thin silica coating cannot withstand the ammonia solution and will also be etched away. To overcome this problem, we performed the etching in the silica coating solution so that silica condensation onto the silver nanoparticle can compensate for the dissolution of silica.

5.3 Latex hollow capsules

In addition to silica nanocapsules, we have also explored the use of polymeric capsules. The polystyrene-acrylic based hollow beads in particular have the advantage that they can be purchased from Polysciences Inc. (Warrington, PA), although their sizes (which are from hundreds of nanometers to one micrometer) are larger than the silica nanocapsules. For applications in which small sizes and good size tunability are important, silica nanocapsules may prove to be more versatile.

Loading of molecules into nanocapsules. We used two methods to introduce molecules into the interior of nanocapsules. The first method is based on a base-swell process (wet method),[75] in which a concentrated stock solution (5.3 % solids in water) of capsules was added directly into a 1-ml solution containing 1.5 mg/ml of fluorescein in 2-propanol/chloroform (95 % / 5 % vol/vol), and 0.02 ml of 30 % ammonia solution. The mixture was sonicated for 15 mins, and the loading process was allowed to proceed at 45 °C for 2 hr. We used this procedure to encapsulate both fluorescein and carbachol into the nanocapsules, in which we first dissolved carbachol in a small amount (< 200 μl) of DI water, then into the 2-propanol/chloroform solution at a final concentration of 12 mg/ml; we dissolved fluorescein directly to the 2-propanol/chloroform solution at a final concentration of 1.5 mg/ml. To separate the nanocapsules from the un-encapsulated fluorescein and carbachol, the suspension was centrifuged at 8,000 rpm for 3 mins and re-suspended in DI water. To ensure complete removal of fluorescein, this procedure was repeated twice with the solution then passed through a size-exclusion column.

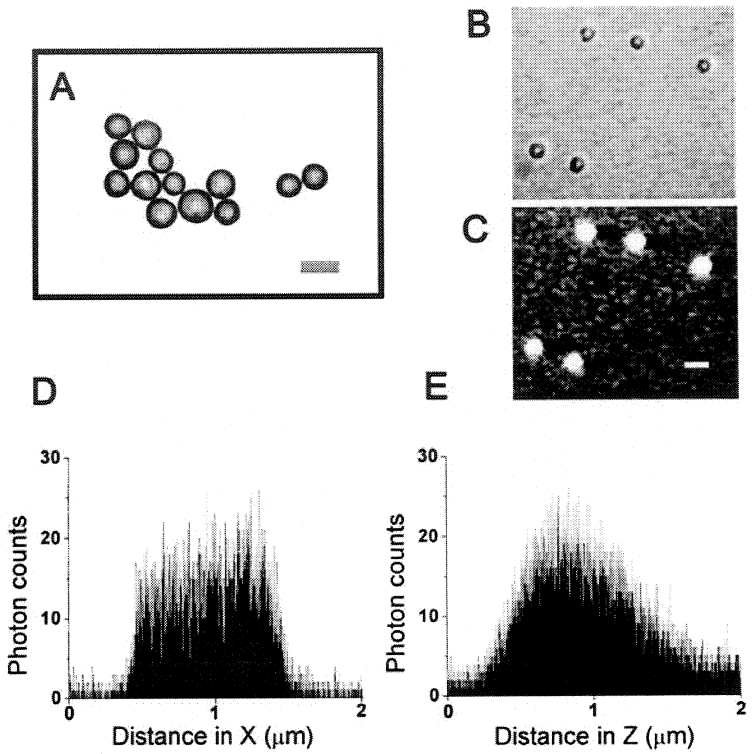

Figure 5-2. TEM, microscopy images and confocal detection of loaded hollow beads. (A) TEM image of polystyrene-based capsules. **(B & C)** Nomarski (**B**) and fluorescence (**C**) images of capsules loaded with fluorescein using the wet method. The scale bar represents 1 μm. **(D & E)** Confocal scans in the xy (**D**) and xz (**E**) dimensions of the fluorescein-loaded capsules.

The second method is based on a dry-swell-dry process (dry method). The stock solution (5.3 % solids in water) of hollow containers was first dried in air then placed in a 60 °C oven for 1 - 2 hours to remove residual water. To introduce fluorescein into the nanocontainers, the dried nanocapsules were placed in a 1-ml solution that contained 1.5 mg/ml of fluorescein in a mixture of 2-propanol and chloroform (95 % / 5 % vol/vol).

The solution was sonicated for 10 to 15 mins to assist the dispersion of the beads into solution. The uptake of fluorescein into the interior of the hollow beads was allowed to proceed overnight, after which the solution was rotary-evaporated until dry, then re-suspended in borate buffer (50 mM, pH 8.5). The suspension of nanocapsules was extensively washed and purified by centrifugation three to four times with borate buffer, then with a size-exclusion column and stored in DI water.

We characterized the latex hollow beads through both TEM and differential interference contrast (DIC) microscope. The DIC images of the capsules were taken with a Nikon TE300 inverted microscope using 100× oil immersion objective (N.A. 1.3). Fluorescent images of the capsules containing fluorescein were obtained with the same microscope, but using the 488-nm line of an Ar^+ laser to excite fluorescence.

Figure 5-2 shows the results of loading of small molecules into the capsules. Figure 5-2A is a TEM image of the capsule, while Fig 5-2B and 5-2C shows the Nomarski and fluorescence images after the capsules had been loaded with fluorescein using the wet method. To ensure fluorescein was loaded inside the capsule and not just attached to the surface of the capsule, we spatially profiled the fluorescence emission from the capsule with confocal microscopy. Figure 5-2D and 5-2E are the xy and xz confocal scans, which clearly show fluorescein is localized inside the capsule. The xy and xz scans appear different because the resolution in the xy, which is defined by the diffraction-limited focus (~ 0.3 μm) of the laser probe volume, is greater than the resolution in the xz, which is determined by the size of the confocal pinhole and the

spherical aberration present in the objective (~ 1 μm). We observed similar spatial fluorescence intensity profiles from capsules loaded with fluorescein using the dry method. The amount of molecules loaded into the capsules can be controlled either by varying the initial concentration of the loading molecules or by varying the size of the capsules.

5.4 characterization of the encapuslation efficiency

We used two methods to visualize the release of fluorescein from individual nanocapsules. In the first method, we released the encapsulated fluorescein using a single focused 3-ns pulse from a N_2 laser (337 nm) to photolyze individual capsules. The subsequent release of fluorescein was monitored under fluorescence imaging with 488-nm wide-field excitation. In the second method, we relied on point detection using single-molecule fluorescence confocal microscopy to monitor the arrival and passage of the released fluorescein. The sequence of steps in this second method is the following: (i) An Nd-YAG laser was used to first optically trap and manipulate a single capsule in solution, (ii) A single pulse from the N_2 laser, which had been aligned co-linear with the focus of the YAG laser, was used to photolyze the capsule and to release the encapsulated fluorescein, and (iii) The diffraction-limited focus of the Ar^+ laser for confocal detection, which was displaced a calibrated distance (e.g. 4 μm) away from the foci of the N_2 and YAG laser, was used to follow the release of fluorescein. The firing of the N_2 laser and

the start of confocal detection were synchronized by the rising edge of a TTL pulse output from an Ortec MCS-PCI data acquisition card (Perkin-Elmer, CA).

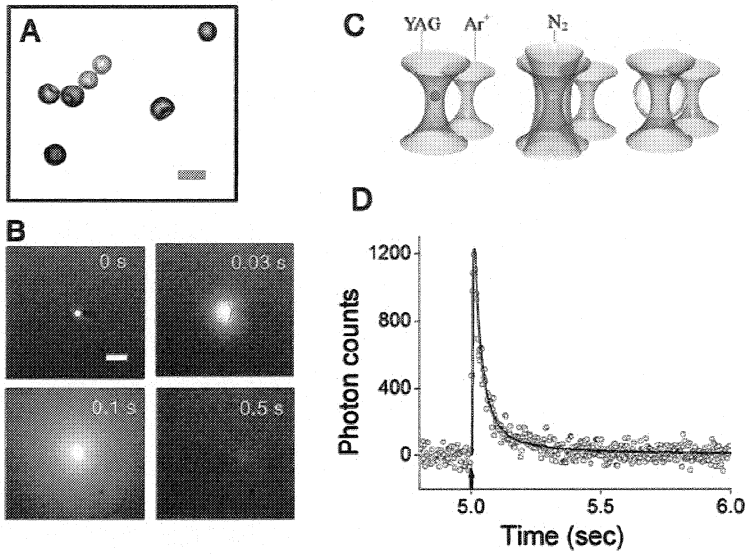

Figure 5-3. Characterization of the encapsulation efficiency of the loaded beads. (A) TEM image of polystyrene-based capsules after loading with fluorescein using the dry method. The scale bar represents 1 μm. **(B)** A sequence of CCD images showing the release of fluorescein upon UV photolysis of the dry-loaded capsules; the solution outside the capsule contained 1 mM NaOH. The scale bar represents 2 μm. **(C)** Schematic illustration of the experimental procedure we used to obtain the result in **(D)**. Here the optically trapped capsule and the confocal probe volume were displaced laterally from each other by 4 μm (left illustration). The capsule was then photolyzed with a single 3-ns pulse at 0.25 μJ from the N_2 laser (middle). The diffusion of fluorescein molecules (expanding green sphere) was monitored with confocal detection (right), which was carried out using the 488-nm line of an Ar^+ laser at 2 mW; data integration time was set at 1 ms. **(D)** Photon trace showing the arrival and passage of fluorescein through the confocal probe volume upon photolysis of capsule and release of fluorescein. Arrow points to the firing of the N_2 laser pulse. The solid line is the simulated result based on the three-dimensional diffusion equation and our experimental conditions.

Figure 5-3A shows a TEM image of the capsule after being loaded with fluorescein using the dry method. Dimples on the surface of the capsule are clearly visible. The exact mechanism of the dimple formation is not clear, but was likely caused by the drying process that resulted in the partial collapse of the shell of the capsule. The presence of the dimple does not, however, seem to negatively affect molecules from being encapsulated into or released from the capsules. In fact, the amount of encapsulated fluorescein was found to be greater using the dry method than with the wet method where no such dimple or deformation was observed.

We monitored the release upon laser photolysis from individual optically trapped nanocapsules using both wide-field fluorescence imaging and confocal point detection. Figure 5-3B is a sequence of fluorescence images showing the release of fluorescein from the capsule. Here a single capsule loaded with fluorescein was first optically trapped, followed by photolysis of the capsule with a single 3-ns pulse from a N_2 laser, the output of which was aligned co-linearly with the trapping laser beam. The observed fluorescence intensity increased as fluorescein diffused away from the volume defined by the capsule because the high concentration of fluorescein present inside the capsule caused it to self quench,[76, 77] and also because the medium contained sodium hydroxide that increased the quantum yield of fluorescein, once it was released from the capsule.

Wide-field fluorescence imaging is a simple and convenient method to visualize the release of fluorescein, but to ensure the observed fluorescence intensity was not caused by excitation from the UV laser pulse, we also used confocal point detection to

monitor the release and diffusion of fluorescein after photodestruction of the capsule. Figure 4-3C schematically illustrates our experiment, in which the diffraction-limited probe volume of the confocal microscope was displaced a calibrated distance (4 μm) away from the co-linearly aligned trapping (YAG) and photolysis (N_2) laser foci in which the capsule is located. Upon photolysis of the capsule, fluorescein began to diffuse away (expanding green sphere in the inset) from the volume defined by the capsule towards the confocal probe volume. Figure 4-3D is the detected photon trace that shows this arrival and passage of fluorescein through the confocal detection volume. The simulated curve (solid line) using a three-dimensional diffusion equation fits well with our experimental observation (Fig 5-3).

To monitor release from nanocapsules, the advantage of using wide-field fluorescence imaging is its ease of use, while confocal detection provides a more sensitive and quantitative measurement. We observed similar signals after photolysis of capsules loaded with the wet method, albeit the amount of fluorescein present was less than it from capsules loaded with the dry method. The drying process increases the loading efficiency, but it also promotes attachment of the molecules to the surface of the capsule, which need be removed with multiple steps of washing and purification. The dry method is useful for applications in which high concentrations of stimuli is required, but for most applications, the wet method may be more appropriate because of the relatively mild conditions under which loading occurs.

5.5 Conclusions

In comparison to caged compounds, nanocapsule-based chemical delivery is versatile and easy to implement from a design and synthetic perspective. Capsules that are hundreds of nanometers to micrometers in diameter are most suitable for *in vitro* studies in which individual capsules can be optically manipulated and photolyzed to release the chemicals for studying specific biological responses. For *in vivo* experiments or brain slices, capsules that are tens of nanometers in diameter are likely more useful. To attain high spatial resolution in such applications, it would be necessary to also develop chemistry for sensitizing the shell of the nanocapsule with the desired molecules, such as dyes having good two-photon absorption cross sections so the nanocapsules can be photolyzed selectively using multi-photon excitation. In comparison with lipid vesicles, the main advantage to the use of silica and polystyrene-based capsules is their inherent robustness that lends themselves to long-term storability, which is pertinent in making this technique easy to use and widely adopted. The drawback with our current methods of loading is the inability to encapsulate large compounds, such as protein and DNA molecules. This drawback may be overcome by loading such large molecules during the synthesis of hollow particles, provided the conditions are sufficiently mild to retain biological functionality. Besides the study of cell signaling, polymeric capsules of micro- and nano- meter dimensions are broadly useful in applications such as drug delivery, gene therapy, and catalysis.

Chapter 6 Layered Polyelectrolyte-Silica Coating for Nanocapsules

6.1 Intorduction

The application of nanocapsules in biology, chemistry, and material science has greatly accelerated in recent years, owing to their ability to encapsulate a wide range of guest molecules,[63, 78] and the flexibility by which their composition, structure, and surface property can be tuned. We have recently employed nanocapules to deliver defined packages of stimuli to single cells with both high spatial (sub-micrometers) and temporal (sub-microseconds) resolutions.[9] In using nanocapsules, one potential issue is uncontrolled leakage and long-term storability. Surface modification and coating has long been recognized as a key parameter in determining the functional performance of nanocapsules, especially in pharmaceutical applications. Most efforts, however, have focused on improving the ability to regulate the fate of the capsules in vivo,[19, 79, 80] on the ease by which they can be dispersed in aqueous solution,[81, 82] and the ability to trigger release with a defined physical or biological signal.[18, 19, 63] Here we describe our development of a general strategy to coat nanocapsules with layered polyelectrolytes and silica to minimize uncontrolled leakage from nanocapsules and to improve their long term storability.

Polyelectrolyte (polyE) and silica are two of the most popular materials used to modify surfaces. PolyEs have been employed in a variety of applied fields, such as in paper making,[83] water treatment,[84] in the paint and food industry,[85] for separation in the mining industry,[86] and in medical science.[87, 88] PolyEs have also been used to flocculate bacteria[89] and for removing trace amounts of ions from aqueous solutions. The strong

interaction between polyEs and the target surface, which can be electrostatic, van der Waals, polymer bridging, or steric stabilization,[90-93] has rendered polyEs a robust coating for a variety of surfaces, including metal, ceramic, and polymer. Several drawbacks, however, are associated with the use of polyE as coating material: (1) A single layer of polyE is thin, on the order of a few nanometers,[93, 94] and deposition of multiple layers is required to form a thicker coating, (2) The permeability of polyE coating can be high;[95-101] for example, it only takes about 10 mins for dyes to leak through a 18-layer-polyE coating,[99] and (3) It is often tedious to coat nanocapsules with many layers of polyE.[102]

Similar to PolyE, silica coating has been widely used to disperse colloidal particles, and has been employed in solar cells,[103] electrochromic devices,[104] electroluminescent films,[105] nonlinear optical switches,[106] and in high-density information storage systems.[107] Silica coatings are robust,[108] water soluble, and can prevent or minimize the aggregation of the coated particles. Silica is also optically transparent,[109] biocompatible, and the thickness of silica coating can be well controlled.[110] Silica, however, cannot be coated on all surfaces. Several reports, for example, showed silica prefers positively charged surfaces and metal surfaces, [109-111] whereas it is difficult to coat negatively charged polymer surfaces, such as polystyrene.[110] To enhance coating for polymer surfaces, silane- or thiol- coupling agents are often required, which involves complicated chemical reactions.[112]

To overcome the limitations of PolyE and silica coating and to retain their respective advantages, we explored a layered PolyE-silica architecture. Here we take

advantage of the tenacious attachment of PolyE to most surfaces, the controlled growth of silica on PolyE, and the good mechanical strength and low permeability of the silica layer to prevent leakage from nanocapsules. We demonstrate this strategy using polystyrene beads and hollow capsules with surfaces that cannot be coated directly by silica. Using this layered coating, we show nanocapsules can be stored for at least one month (our period of observation) without measurable leakage of their contents. This layered architecture also permits the formation of thick (> 100nm) layers of silica that are otherwise difficult to generate. Although this paper focuses on the growth of silica on PolyE, we believe this strategy can also be applied to the growth of other types of molecular layers on PolyE.

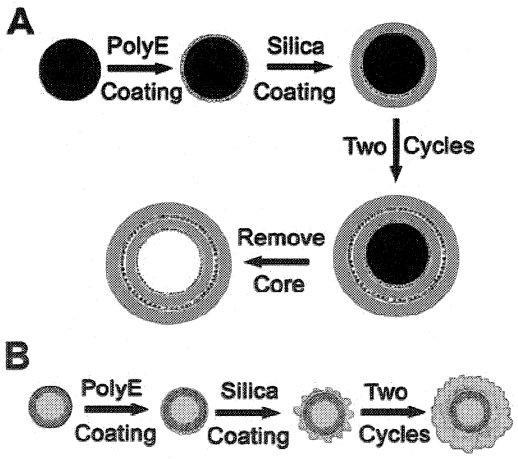

Figure 6-1. Schematic illustrating our strategy for coating two layers of polyelectrolyte and silica on polystyrene beads (A) and latex nanocapsules (B). Each layer of polyelectrolyte was formed by first depositing PDADMAC (positively charged), followed by PSS (negatively charged), and finally with PDADMAC. PDADMAC: Poly(diallyldimethylammonium chloride); PSS: poly(styrenesulfonate).

6.2 Coating and characterization of polystyrene beads and latex capsules with polyE-silica

Coating of polystyrene beads ---- surface modification with polyelectrolyte. We used polyelectrolyte multilayers as an initial coating layer or "adhesion modifier" to enhance the growth of silica on polystyrene beads. Positively charged poly(diallyldimethylammonium chloride) (PDADMAC, M.W. 100,000-200,000) and negatively charged poly(styrenesulfonate, sodium salt) (PSS) were used to form PDADMAC/PSS/PDADMAC-three-layer coating on polystyrene beads (1 μm in diameter). In a typical procedure, stock solution of 0.01-mL polystyrene beads (2.6 % solid in water) was suspended sequentially in each of the 1-mL polyelectrolyte solution (1 mg/mL in 0.5 M NaCl) for 20 mins. After each suspension in the polyelectrolyte solution, the beads were pelleted down at 7,000 rpm for 3 mins and then re-suspended in a new polyelectrolyte solution by vortexing or sonication. Prior to silica coating, the polyE-coated beads were washed three times with de-ionized (D.I.) water; the beads were isolated after each wash by centrifugation at 7,000 rpm for 3 mins.

Coating of polystyrene beads ---- growth of silica on polyelectrolyte layers. The polyE-coated beads were dispersed in a solution containing 10-mL iso-propanol, 1.75-mL D.I. water, and 0.25-mL ammonium hydroxide (at a 1:10 dilution with D.I. water). While this solution was being stirred, we introduced drop-wise 80-μL of tetraethylorthosilicate (TEOS). The growth of the silica layer was allowed to proceed for three hours under continuous stirring. To terminate further growth of silica, the beads

were first isolated from solution by centrifugation at 5,000 rpm for 3 mins, then washed three times with DI water as described above. To form another coating of PolyE and silica, we repeated the above procedure under identical conditions.

Formation of silica capsules. To measure the thickness of the PolyE-silica coating, we removed the polystyrene core either by calcinations at 450 °C (Furnace 1300, Thermolyne, Sigma-Aldrich, Milwaukee, WI, USA) for 1 Hr; or by soaking the particles (pre-dried in a 60 °C oven) in tetrahydrofuran (THF) for 4 Hrs.

Loading of latex nanocapsules. To load nanocapsules, which are composed of a polystyrene-acrylic copolymer with a tunable diameter from 0.4 μm to 1 μm, we mixed 25 μL of the stock solution that contained the capsules with 3 mL of loading solution, which contained 1.9-mg/mL fluorescein in 2-propanol/chloroform (95%/5% (v/v)). To disperse the capsules in solution, the mixture was sonicated and vortexed till the beads were fully dispersed; the loading was then allowed to proceed at 50 °C for 2 Hrs under continuous stirring. To terminate loading, we centrifuged the mixture at 8000 rpm for 3 mins, then discarded the supernatant. The pellet of beads was washed repeatedly (3-4 times) with a solution containing borate buffer (50 mM at pH 8.5) and 2-propanol at a ratio of 4:1 (v/v), then again with D.I. water (3 times). After each wash, the beads were isolated from solution by centrifugation at 10,000 rpm for 3 mins.

Polyelectrolyte and silica coating of loaded nanocapsules. The loaded nanocapsules were coated using the same procedure we described for the coating of beads. Silica coating was carried out in a solution containing 0.45-mL iso-propanol, 20-

μL DI water, 25-μL ammonium hydroxide (1:10 dilution with D.I. water), and 10-μL TEOS for 1.5 Hrs under continuous stirring. The coated capsules were isolated by centrifugation and washed three times with D.I. water.

Characterization of loading into and leakage from nanocapsules. We loaded fluorescein into the nanocapsules and quantified the amount of loaded fluorescein using fluorescence imaging, then followed the release of fluorescein from both coated and uncoated nanocapsules over 30 days. To visualize the amount of loaded fluorescein inside the capsules, we added ammonium hydroxide into the solution that contained the capsules, which increased the pH both outside and inside the capsules and rendered the fluorescein within the capsules fluorescent. We imaged the fluorescence from individual capsules using epi-illumination (excitation at 488nm with an Ar^+ laser) and a high sensitivity cooled CCD camera (Cascade 512B from Roper Scientific, Duluth, GA). To monitor release from nanocapsules, we stored the capsules in airtight quartz cuvettes to prevent evaporation of solution. Release was monitored by measuring the fluorescence (Luminescene Spectrometer, LS50B, Perkin Elmer Inc., Wellesley, MA) of the solution in 50-mM borate buffer (pH 8.5).

Laser-induced release from individual nanocapsules. We focused a single pulse (3ns at 337nm) from a N_2 laser onto a loaded and coated nanocapsule (1 μm in diameter) to trigger the release from the capsule. The release of molecules (fluorescein) from the capsule was monitored using single-molecule confocal detection. Details of this procedure and setup have been described elsewhere.[49] Briefly, the output of a N_2 laser

(VSL-337ND-S, Laser Science Inc., MA; wavelength at 337 nm with pulse duration of ~ 3 ns) was used to photolyze single capsules and to trigger release. To follow the release of fluorescent molecules from the photolyzed capsule, the output of an Ar^+ laser (Stabilite 2017, Spectra-Physics, CA; wavelength at 488 nm) was tightly focused and positioned in close proximity to the capsule prior to photolysis so as to excited fluorescence from the released molecules as they transited this laser focal volume; detection of the emitted photons was carried out with an avalanche photodiode (SPCM, Perkin-Elmer Inc., Wellesley, MA) using the confocal configuration.

Chemicals and materials. Poly(diallyldimethylammonium chloride) (PDADMAC) with a molecular weight (MW) of 100,000-200,000, poly(styrenesulfonate, sodium salt) (PSS), and tetraethylorthosilicate (TEOS) was purchased from Sigma-Aldrich (Milwaukee, WI). Fluorescein was obtained from Molecular Probes (Eugene, OR), and polystyrene beads and hollow latex capsules were from Poly Sciences Inc. (Warrington, PA). All the other chemicals were from Fisher Scientific (Fair Lawn, NJ).

6.3 Results and discussion

Polyelectrolyte/silica coating on polystyrene beads. The surface of polystyrene beads is negatively charged, owing to the presence of sulfate ester groups. To coat this negatively charged surface with silica, we used polyelectrolytes (polyEs) as an adhesive layer and employed the Stöber method[113] to grow silica directly onto these polyE layers (Figure 6-1).

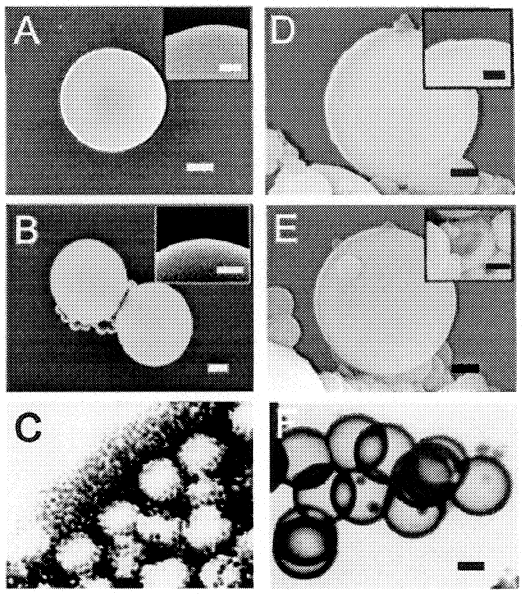

Figure 6-2. SEM and TEM images of polystyrene beads. (A) SEM image of polystyrene beads prior to any coating. (B) SEM image of polystyrene beads after direct silica coating without the deposition of polyelectrolyte layers. (C) TEM image of the silica coating (with no polyelectrolyte layers) after removal of the polystyrene core with calcinations at 450 °C for 1 Hr. Rather than forming a smooth layer of silica, the absence of polyelectrolyte layers in (B) and(C) resulted in the formation of free silica particles that were attached to the surface of the beads. (D) SEM image of polystyrene beads after deposition of two layers of polyelectrolyte-silica coating. (E & F) SEM (E) and TEM (F) images of the polyelectrolyte-silica capsules after removal of the polystyrene core by etching in tetrahydrofuran for 4 Hrs. The insets in (A) – (E) show enlarged portion of the images in the respective panels; the inset in (E) shows SEM image of a cracked polyelectrolyte-silica capsule. The scale bars represent 250 nm in the SEM images and 400 nm in the TEM images; the scale bars in the insets of panels (A) – (D) represent 100 nm and the scale bar in the inset of panel E represents 500 nm.

Figure 6-2 shows scanning electron microscope (SEM) and transmission electron microscope (TEM) images that summarize the effects of coating polystyrene beads with silica without PolyE layers (Figure 6-2A~6-2C) and with PolyE layers (Figure 6-2D~6-2F). Figures 2A and 2B are SEM images showing the appearance of polystyrene beads

before and after coating with silica. Prior to silica coating (Figure 6-2A), the beads had a smooth surface. After silica coating (Figure 6-2B), the beads were decorated with silica particles. Without PolyE layers, silica could not attach to the surface of polystyrene and thus underwent a homogeneous nucleation process[114] to form silica particles. To further examine the effect of direct silica coating, we removed the polystyrene core by calcinations and obtained TEM images of this sample (Figure 6-2C), in which the silica particles at the surface of the beads can be clearly discerned. The circular cavities in Figure 6-2C indicates the empty space left behind from removal of the polystyrene beads.

In contrast to the inability of silica to grow directly on polystyrene surfaces, the presence of polyE adhesive layers greatly enhances the growth of the silica layer on the polystyrene beads (Figure 6-2D~6-2F). To introduce positive charges onto the polystyrene surface, we modified the surface first with a layer of PDADMAC (positively charged), followed by a layer of PSS (negatively charged), and finally with another layer of PDADMAC. Figures 6-2D and 6-2F present results of the subsequent growth of silica onto this polyE layer (i.e. PDADMAC/PSS/PDADMAC) via a heterogeneous process.[47]

Figure 6-2D shows an SEM image of a bead coated with two cycles (i.e. two layers of PDADMAC/PSS/PDADMAC-silica) of polyE and silica, whereas Figures 6-2E and 6-2F are SEM and TEM images of the two-layer polyE-silica coating after the polystyrene beads had been etched away by THF. The presence of polyE-silica coating is marked by surface texture (see Figure 6-2D inset) and by the increase in size of the beads (Figure 6-2D), which can be verified by the direct observation of the polyE-silica shell

after removal of the polystyrene core (Figure 6-2E inset and Figure 6-2F). The homogeneity of the two-layer polyE-silica coating is evident in Figure 6-2F. The presence of silica greatly increased the mechanical strength and robustness of the coating, and deformations (folds and creases) that occur for capsules composed solely of multiple layers of polyE[102, 115] were effectively eliminated.

Thickness of the polyE-silica coating. Thickness is an important factor that determines the property and function of the coating, such as its robustness and permeability. To study the thickness of our coating, we mechanically disrupted the integrity of the polyE-silica coating by grinding, then imaged the cross sectional appearance of the coating with SEM (Figure 6-3).

Previous studies show that the thickness of silica layer is usually limited to less than 100 nm. Within this range, the thickness can be tuned by controlling the duration or condition (e.g. pH) of silica growth or by adjusting the concentration of silicate.[37 109] Silica layers that are much thicker than 100 nm are difficult to achieve, because further extending the time of coating will lead to a smoother layer of silica but will not increase its thickness. Increase in the amount of silicate will accelerate the undesired homogeneous nucleation process and generate free silica particles rather than increase the thickness of the coating.[73, 114]

A layered-polyE-silica architecture provides a convenient route to create thick layers of silica. After two cycles of polyE deposition and silica growth, we obtained a coating thickness of 128 nm ± 7 nm (N = 15) based on SEM measurements. Even thicker

layers of coating can be reached by repeating this cycle of polyE deposition and silica growth.

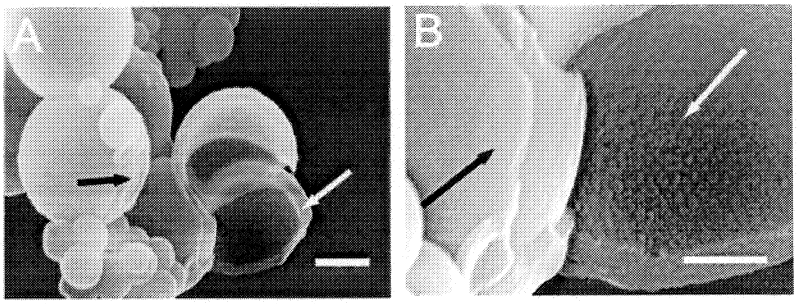

Figure 6-3. SEM images of cracked polyelectrolyte-silica capsules, which were formed by two cycles of polyelectrolyte deposition and silica growth; the capsules were cracked by grinding. The white arrow points to the thickness of the two-layer polyelectrolyte-silica coating, which we measured to be 128 nm ± 7 nm (N = 15); the black arrow points to the layered onion-like character of this two-layer coating, in which a small portion of the outer layer (i.e. second layer of polyelectrolyte-silica) was peeled from the inner layer (i.e. first layer of polyelectrolyte-silica) during the grinding and cracking of the capsules. Silica growth was allowed to proceed for 3 Hrs, which resulted in a smooth coating of silica. (B) is an enlarged image of (A), where the scale bar in (A) represents 500 nm and the scale bar in (B) represents 200 nm.

The polyE-silica coating has a layered architecture and exhibits an onion-like behavior. When the two-layer polyE-silica coating was fractured with force, we occasionally observed under SEM the peeling of one layer from the second layer (see black arrows in Figure 6-3). The thickness of one such layer is about half that of the two-layer coating. This observation also indicates the coating was well performed and homogeneously applied to the surface of polystyrene beads when polyEs were used.

In Figure 3B, the inner and outer surfaces of the capsule show distinct differences in texture. The inner surface, from which the coating started to grow, shows a bumpy and rough texture; this roughness was likely caused by the limited aging time of the inner silica layer.[44, 45] In contrast, the outer silica layer appears smooth, because the outer layer was allowed to age for ~ 3Hrs. We see a patchy and rough outer silica layer when the aging or coating time was reduced to 1.5 Hrs (see discussions accompanying Fig 4).

We have successfully applied PolyE-silica layers for coating polymer surfaces that were otherwise difficult to coat with silica alone. By etching away the polymer core, this type of polyE-silica coating can also form hollow capsules with thick and mechanically robust shells (Figure 6-2F and Figure 6-3). More importantly, this layered coating can form an effective seal to prevent undesired leakage from nanocapsules.

Coating of PolyE and silica on latex capsules. Previously, we have used hollow latex nanocapsules to confine physically the bioactive molecules of interest within the core of the capsules.[49] Using a single nanosecond laser pulse, we could achieve spatially (with sub-micrometer resolution) and temporally (with sub-microsecond resolution) resolved release from individual capsules onto single biological cells.[9, 49] We believe the use of nanocapsules as "physical cages" will complement the use of chemical cages for a wide range of biological studies. One determining factor in making this technique easy to use and widely adopted in the biological community is the long-term storability of loaded nanocapsules. We observed latex capsules to be stable within days, but over longer periods of time, we have noticed slow leakage of the contents from such capsules

into solution. One of our main motivations in developing this layered PolyE-silica coating is to prevent such leakage and to improve the long-term stability of loaded nanocapsules.

Figure 6-4 shows SEM and TEM images of the polyE-silica coated latex nanocapsules. Similar to polystyrene beads, these nanocapsules cannot be coated directly with silica, owing to the presence of negative charges on the surface of the capsules. Panels 6-4A and 4B show SEM images, respectively, of native capsules and results of our attempts to apply direct silica coating on the capsules. Rather than being coated with a silica layer, we observed the formation of free silica particles as we did with polystyrene beads. We then coated the capsules with three layers of polyE (PDADMAC/PSS/PDADMAC) (Figure 6-4C). The presence of the positively charged PDADMAC layer makes subsequent silica deposition and growth more effective (Figure 6-4D).

The conditions we used to coat polyE and silica layers, which involve high ionic strength solution for polyE deposition (0.5 mM NaCl) and organic solutions for silica growth (2-propanol), have the potential to cause the encapsulated molecules to leak out from the capsules. To quantify this potential leakage during our coating procedure, we have carried out two control experiments: (1) We soaked the fluorescein loaded capsules in 0.5 mM NaCl and borate buffer (pH 8.0), the same ionic strength as we used for polyE deposition. After 20 Hrs of soaking, which was much longer than the duration we used

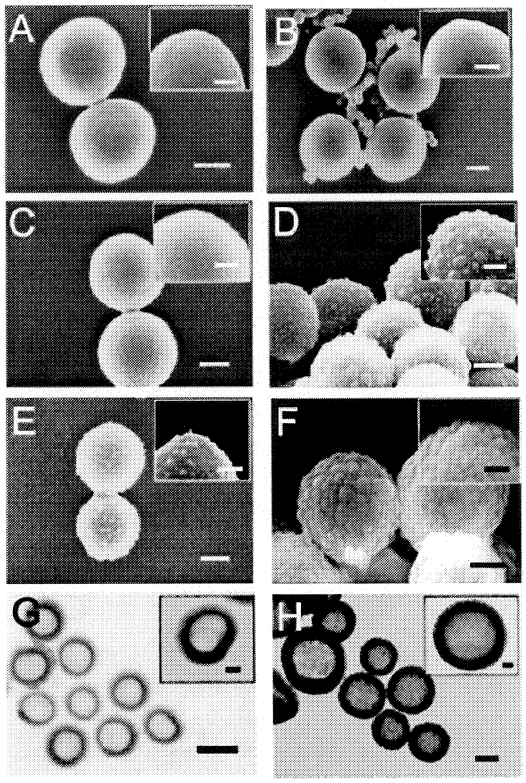

Figure 6-4. SEM and TEM images of latex nanocapsules. SEM image of uncoated capsules (A), after direct silica coating without the deposition of any polyelectrolyte layers (B), after deposition of one layer of polyelectrolyte consisting of PDADMAC/PSS/ PDADMAC (C), after one cycle of polyelectrolyte deposition and silica coating (i.e. PDADMAC/PSS/ PDADMAC – silica) (D), after deposition of another layer of polyelectrolyte on the first layer of polyelectrolyte-silica coating (i.e. PDADMAC/PSS/ PDADMAC – silica – PDADMAC/PSS/ PDADMAC) (E), and after two cycles of polyelectrolyte deposition and silica coating (i.e. PDADMAC/PSS/ PDADMAC – silica – PDADMAC/PSS/ PDADMAC – silica) (F), Silica growth was allowed to proceed for only 1.5 Hrs, which resulted in the patchy appearance of the silica layers. (G & F) are TEM images of latex nanocapsules prior to any coating (G) and after two cycles of polyelectrolyte-silica coating (H). The insets show enlarged portion of the images in the respective panels. The scale bars in panels (A) – (F) represent 200 nm, and in panels (G) and (H) they represent 400 nm; the scale bars in all insets represent 100 nm. PDADMAC: Poly(diallyldimethylammonium chloride); PSS: poly(styrenesulfonate).

for polyE deposition, we still did not observe any measurable leakage from the capsules, and (2) We soaked the polyE coated capsules in the organic solution we used for subsequent silica growth after polyE deposition. After three hours, we observed approximately ~ 3 % loss from the loaded capsules coated with three layers (PDADMAC/PSS/PDADMAC) of polyE; the loss from uncoated capsules was ~ 10 %.

Although the loss from capsules in the organic solution was only ~ 3 % over a three-hour period, to further minimize such leakage we decreased our silica coating times from 3 Hrs to 1.5 Hrs. This reduced coating time caused the latex surface to appear slightly patchy (Figure 6-4D), but this patchy surface was smoothened with another cycle of polyE deposition (Figure 6-4E) and silica growth (Figure 6-4F). Figures 6-4G and 6-4H shows TEM images of the capsules prior to coating (Figure 6-4G) and after two cycles of polyE deposition and silica coating (Figure 6-4H).

Characterization of loading efficiency for uncoated and coated nanocapsules. We have characterized the homogeneity of loading into nanocapsules and compared the relative amount of loaded molecules between uncoated and coated capsules. Figure 6-5 summarizes our result. Panels 6-5A and 6-5D are bright-field images of uncoated and coated capsules (0.55 μm in outer diameter) loaded with 1.9-mM fluorescein, whereas panels 6-5B and 6-5E are the corresponding fluorescence images. The coated capsules contained two layers of polyE and silica, that is, they underwent two cycles of coating.

To determine the variation in the number of encapsulated fluorescein molecules, we analyzed the fluorescence images and measured the total fluorescence intensity from

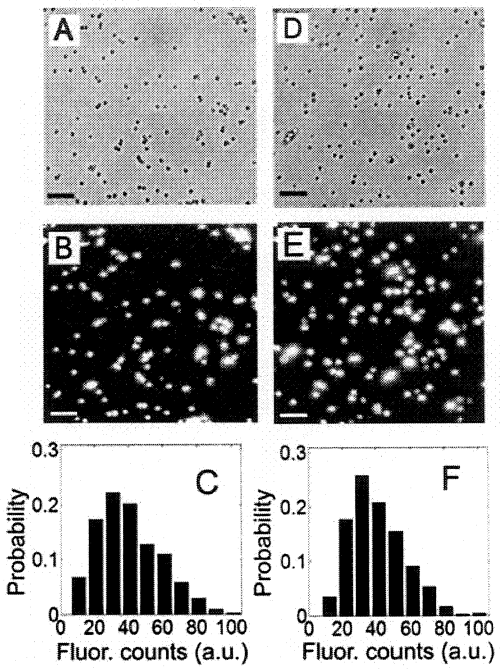

Figure 6-5. Characterization of loading of fluorescein into latex nanocapsules (with outer diameter of 0.55 μm) that were uncoated (A – C) and coated with two cycles of polyelectrolyte-silica deposition (D – F). (A & B) are bright-field and fluorescence images of uncoated nanocapsules loaded with fluorescein; (D & E) are the corresponding bright-field and fluorescence images of loaded nanocapsules coated with two layers of polyelectrolyte-silica. (C & F) are histograms showing the variation in the amount of fluorescein loaded into uncoated and coated nanocapsules. The probability indicated on the y-axis was obtained by normalizing the number of capsules of a given fluorescence intensity against the total number of capsules analyzed, which consisted of 447 uncoated and 547 coated capsules. The observed spread in the number of loaded molecules among the capsules was caused by variation in the volume of the capsule cavity, which was measured to be $9.99 \pm 2.95 \times 10^{-21}$ m^3 from TEM images. The scale bars in all images represent 4 μm; a.u. represents arbitrary units. The fluorescence images were acquired with 100-ms integration times and with a camera gain setting of 3200. (A) and (B) are bright field and fluorescence images of uncoated nanocapsules, and the scale bars represent 4 μm; (D) and (F) are bright field and fluorescence images of coated nanocapsules with two-layers of polyE-silica structure, and the scale bars represent 4 μm. (C) and (F) are histograms of the probability of uncoated and coated capsule population as a function of fluorescence counts measured by a cascade camera responding. The fluorescence images were acquired with 100ms integration times with a gain setting of 3200.

each individual capsules. Panels 6-5C and 6-5F are histograms showing the results of this measurement for 447 uncoated capsules and 547 coated capsules. The variation in the amount of encapsulated fluorescein was comparable for both coated and uncoated samples, which indicated that the coating procedure did not adversely affect the homogeneity in the number of loaded fluorescein molecules. The origin of this variation, we determined, was caused by the spread in the volume of the nanocavity within the capsule, which had a distribution of $(9.99 \pm 2.95) \times 10^{-21}$ m^3 as determined from our TEM images. We found the loading and coating processes themselves introduced negligible variation in the number of contained molecules among the capsules.

Characterization of leakage fromcoated capsules. We monitored leakage of encapsulated fluorescein from both uncoated and coated nanocapsules over 30 days. Here the capsules were stored in airtight quartz cuvettes and we monitored with a fluorimeter the amount of fluorescein that leaked into solution after the capsules were sedimented to the bottom of the cuvette. Figure 6-6 shows the results, in which non-coated capsules showed significant leakage and the coated capsules exhibited no detectable leakage over this 30-day period. Because we did not remove the fluorescein molecules that leaked from the capsules from solution, leakage from the uncoated capsules reached equilibrium after two weeks, that is, the number of fluorescein that left the capsule equaled the number that entered the capsules. In contrast, the amount of fluorescein that leaked from capsules coated with two layers of polyE-silica was within the noise of our measurement.

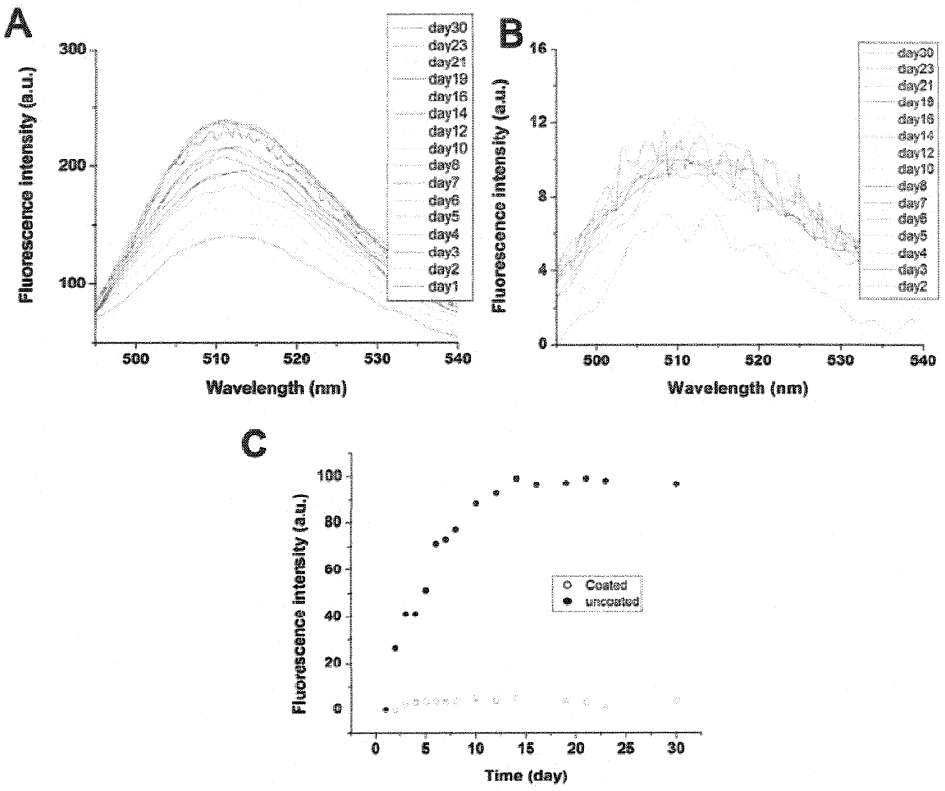

Figure 6-6. Monitoring leakage of loaded fluorescein over a 30-day period from latex nanocapsules (with outer diameter of 0.55 μm) that were uncoated (A) and coated with two layers of polyelectrolyte-silica (B). (A & B) are raw fluorescence spectra of the fluorescein molecules that leaked into solution from the capsules; the solution containing the capsules were stored in airtight quartz cuvettes, and the spectra were taken after the capsules were allowed to sediment to the bottom of the cuvette and out of the beam path of the excitation light. Note the large difference in the scale of the observed fluorescence intensity from uncoated (A) and coated (B) capsules. (C) plots the changes over time in the observed fluorescence intensity at 510 nm (see lines marked in (A) and (B)) caused by leakage of fluorescein into solution from capsules there were uncoated (●) and coated with two layers of polyelectrolyte-silica (○). The capsules were stored in 50-mM sodium borate at pH 8.5. Excitation was carried out at 488 nm, and the slit width was set at 2.5 nm for both excitation and emission.

Laser-triggered release of the loaded molecules. We have demonstrated previously that molecules encapsulated within the latex nanocapsule can be released selectively with the application of a single nanosecond UV laser pulse. [49] Here we wanted to verify that we can achieve similar laser-triggered release using coated nanocapsules. Figure 6-7 shows laser-triggered release from a single optically trapped nanocapsule that was coated with two layers of polyE-silica, in which the release of fluorescein was monitored by a confocal detection volume placed ~ 5 micrometers away from the capsule. The sharp rise in our detected number of photons (Figure 6-7) signaled the arrival of fluorescein at the confocal detection volume after fluorescein molecules were released from the capsule; the subsequent decay in photon counts was caused by dilution in the number of released fluorescein molecules as they transited the detection volume away from point of release. [117]

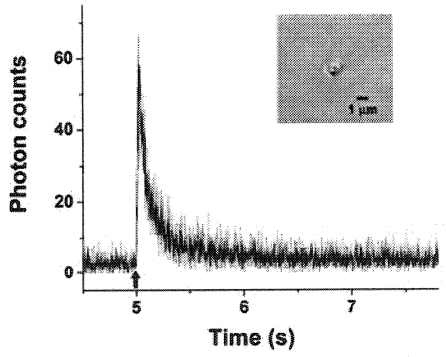

Figure 6-7. Laser-triggered release of fluorescein from a single optically trapped latex nanocapsule, which was coated with two layers of polyelectrolyte-silica. A single 3-ns laser pulse at 337 nm photolyzed the trapped capsule and released the contained fluorescein molecules, which were monitored by confocal detection. The recorded time trace of photon counts signaled the arrival and passage of the released fluorescein at the confocal probe volume that was placed ~ 5 μm from the capsule. Arrow on the time trace marks the firing of the N_2-laser pulse. The inset shows the trapped capsule prior to being photolyzed.

6.4 Conclusion

While polyelectrolyte and silica have been both widely used for coating surfaces, few efforts have focused on the use of polyelectrolyte layers to enhance the growth of other charge-sensitive molecular layers. This paper demonstrates polyelectrolyte does form excellent adhesive layers and that silica can be grown directly on polyelectrolyte-modified surfaces. This layered polyelectrolyte-silica architecture has several advantages for coating nanocapsules: (1) The coating can be applied to all surfaces that can be modified with polyelectrolyte layers, (2) The thickness of the layered coating can be controlled in principle over a wide dynamic range by increasing the number of layers, (3) The presence of silica in the layered structure makes the coating mechanically robust, (4) This layered coating forms effective seals to prevent unwanted leakage from loaded capsules and increases drastically the storability of loaded nanocapsules, (5) The coating procedure does not cause significant leakage from the capsules or variation in the number of loaded molecules, and (6) The coating does not adversely affect the release of loaded molecules from capsules using single-pulse laser trigger. Although this paper focuses on developing coatings for nanocapsules and the growth of silica on polyelectrolyte, we believe this strategy can be applied to the growth of other types of molecular layers on polyelectrolyte for creating a wide range of layered nanoscale architectures.

Chapter 7 Photolysis of capsules

7.1 Introduction

To test the photolysis time scale, we designed a new strategy for initiating a chemical reaction that is based on the laser-induced breakdown of a nanoscopic barrier, which physically separates the reactants in space. Based on our test, the breakdown time is around 0.3 μs. Because the breakdown of the barrier is fast and owing to the nanometer dimension of the barrier, the reactants can be brought together and the reaction can be initiated rapidly. The timescale most suited for this method (from microseconds to tens of milliseconds) bridges nicely between the faster time scales that are accessible mostly with laser-based triggering experiments and the slower time scales that are studied most frequently with flow-based devices.

7.2 Importance of chemical kinetics

Chemical kinetics is central to biological processes from protein folding to signal transduction and enzyme catalysis.[118-123] To access fast kinetics, it is necessary to trigger the reaction rapidly and with a sharp time distribution, which typically means an initiation time that is much shorter than the half-life of the reaction.[124] Most common strategies for initiating a chemical transformation in solution fall into the following three categories: (1) Flow-based mixing techniques[124-127] (e.g. stopped flow), (2) Relaxation-based methods[124, 128-130] (e.g. temperature or pressure jump), and (3) Photochemical triggering[131-133] (e.g. flash photolysis). Of these methods, flow-based mixing techniques are perhaps the most common, owing to their ease of use and implementation. Recent

advances in microfluidics have dramatically improved the time scale of this method from the millisecond range[7] to tens of microseconds.[125, 127] Here we present a new strategy for initiating a chemical reaction that is based on the laser-induced breakdown of a nanoscopic barrier, which physically separates the reactants in space. The permeability of lipid membrane can be altered by a wide range of physical methods, including the use of ionic strength, pH, temperature, ultrasound, and light.[19, 134, 135] In particular, UV light has been used to alter membrane permeability by changing the conformation of the UV-sensitive groups in the membrane (e.g. cis-trans isomerization)[136, 137] or by changing the packing of the lipid bilayer upon UV polymerization.[138, 139] Pulsed UV laser has also been used to fuse lipid vesicles and to ablate biotissue and polymer.[9, 27, 140] In our experiments, we used single UV laser pulse to photolyze individual lipid vesicles doped with UV sensitizers in the membrane. Because the breakdown of the barrier is fast and owing to the nanometer dimension of the barrier, the reactants can be brought together and the reaction can be initiated rapidly.

7.3 Implementation of our strategy

Figure 7-1 illustrates our strategy, in which reactant A is confined to the interior of a lipid vesicle and is thus physically separated by the nanometer thick lipid membrane

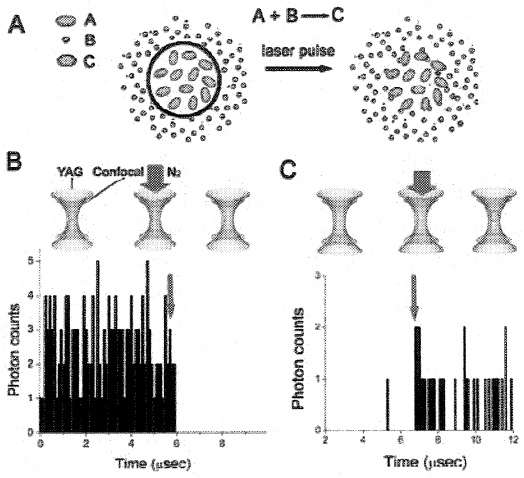

Figure 7-1. **Illustration of our experimental setup.** Three laser beams (YAG at 1064 nm; Ar^+ laser at 488 nm; N_2 laser at 337 nm) were directed into a high numerical aperture objective (N.A. 1.3) of the microscope using a set of dichroics; fluorescence signals were collected through the same objective and detected. The enlarged image shows our experimental strategy, in which a single N_2 laser pulse (3-ns duration) disrupts the partition defined by the membrane bilayer. Once the partition is compromised, the reactants denoted by A and B are permitted to encounter each other and react to form the product C. M, mirror; DC, dichroic; OJ, objective; CS, coverslip.

from reactant B, which is located outside the vesicle. Upon photo-destruction of this membrane by a single UV-laser pulse, reactants A and B are permitted to encounter each other to form the product C. As Figure 1 depicts, our experiment requires the use of three lasers: a YAG laser for the optical manipulation of vesicle, an Ar^+ laser for confocal

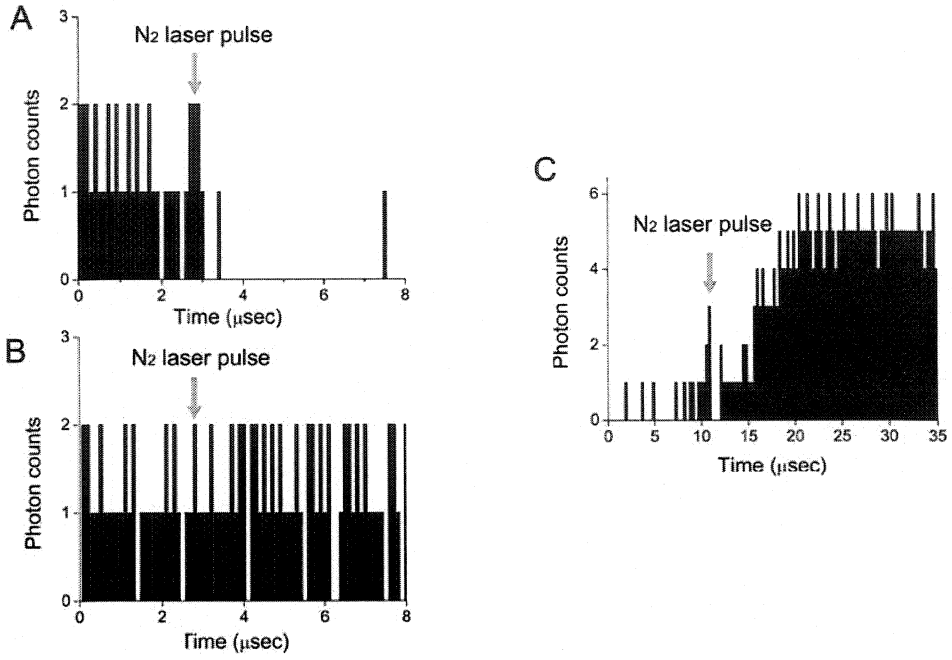

Figure 7-2. **Characterization of the timescale of laser photolysis.** (A) Photolysis of a lipid vesicle that was doped with 5% (by weight) of a pyrene-based UV absorptive lipid (1-hexadecanoyl-2-(1-pyrenedecanoyl)-*sn*-glycero-3-phosphocholine, β-py-C_{10}-HPC) as well as 0.1% (by weight) of a green fluorescent membrane dye (3,3'-dioctadecyloxacarbocyanine perchlorate, DiO-C_{18}). Arrow marks the arrival of the UV laser pulse onto the vesicle; each bin in the time trace corresponds to 100 ns. The CW YAG and Ar^+ lasers were 0.1 W and 1 mW in power, respectively, while the N_2 laser has a pulse energy of ~ 1 μJ; all laser powers were measured prior to the objective. (B) Photolysis of a lipid vesicle that was doped with only 0.1% (by weight) DiO-C_{18} under identical experimental conditions as in (A). (C) Photolysis of a vesicle doped with 5% (by weight) β-py-C_{10}-HPC and containing carboxyfluorescein in acidic pH <2; the vesicle was suspended in 50 mM borate buffer at pH 8. Upon photolysis and membrane breakdown, the carboxyfluorescein inside the vesicle (which was non-fluorescent) became deprotonated and fluorescent. This increase in fluorescence was monitored by confocal detection with the Ar^+ laser (40 μW prior to objective) and an avalanche photodiode. Arrow marks the arrival of the UV laser pulse onto the vesicle; each bin in the time trace corresponds to 300 ns.

detection, and a N_2 laser for photolysis. We used individual lipid vesicles in our experiments for ease of preparation and analysis, but we believe this strategy can be

applied equally well to bulk solution and to systems with other geometries (e.g. free-standing planar lipid bilayers) or for those that use different materials other than lipids (e.g. polymers).

The breakdown time of the lipid membrane, which directly correlates with the initiation time of the chemical reaction, is determined by the duration of the laser pulse and the photolysis efficiency of the material. Figure 7-2 presents the characterization of the timescale for this process. Figure 7-2A shows a time trace for the photolysis of a single lipid vesicle. The membrane of this vesicle was composed of 1,2-Dipalmitoyl-*sn*-Glycero-3-Phosphocholine (DPPC) and 1,2-Dipalmitoyl-*sn*-Glycero-3-[Phospho-*rac*-(1-glycerol)] sodium salt (DPPG) (10:1 by weight), and was doped with 5% (by weight) of a pyrene-based UV absorptive lipid [1-hexadecanoyl-2-(1-pyrenedecanoyl)-*sn*-glycero-3-phosphocholine, β-py-C_{10}-HPC] as well as 0.1% (by weight) of a green fluorescent membrane dye (3,3'-dioctadecyloxacarbocyanine perchlorate, DiO-C_{18}). In the experiment, the individual vesicle was first optically trapped while being monitored continuously in green fluorescence (500-580 nm; from DiO-C_{18}) with a confocal microscope. Upon application of a single 3-ns pulse from the N_2 laser, the vesicle membrane was photolyzed within 0.3 μs (arrow marks the arrival of the UV laser pulse onto the vesicle; each bin in the time trace corresponds to 100 ns) as visualized by the disappearance of fluorescence signal from DiO-C_{18} in the confocal probe volume (DiO is only highly fluorescent when it is incorporated in the membrane). The presence of the

UV dye (β-py-C_{10}-HPC) in the membrane of the vesicle is critical for achieving photolysis of the vesicle.

The disappearance of the fluorescence signal from DiO-C_{18} is caused by the breakdown of the lipid membrane rather than the photobleaching of DiO-C_{18} by the single 3-ns UV laser pulse. Figure 7-2B is a control experiment that shows the attempt to photolyze a single vesicle under identical experimental conditions but with the absence of the UV absorptive lipid. Here the observed fluorescence signal was unchanged after application of the UV laser pulse, which indicated the vesicle was not photolyzed and DiO-C_{18} was not photobleached by the UV laser pulse. From these experiments (Figure 7-2A and 7-2B), we conclude the timescale for the disruption of membrane integrity by a single 3-ns UV laser pulse is on the order of 300 ns under our experimental conditions.

To further examine the time scale of photolysis of the lipid membrane, we monitored the photolysis of a single lipid vesicle containing 250 μM carboxyfluorescein (Figure 7-2C). The interior of the vesicle was not buffered and was in acidic pH (<2), which rendered carboxyfluorescein nonfluorescent; the exterior of the vesicle, however, was composed of a borate buffer at pH 8, which would deprotonate carboxyfluorescein and cause it to be fluorescent once the lipid membrane was photolyzed.[141-143] Here the confocal probe volume was placed at the vesicle membrane (Figure 7-1) and we observed fluorescence signal increase after ~ 1 μs of the firing of the N_2 laser (arrow in Figure 7-2C), thereby indicating the membrane was photolyzed and the reaction was initiated within ~ 1 μs. This longer time scale of ~ 1 μs we observed in Figure 2C in comparison

with the faster membrane photolysis times of ~0.3 μs in Figure 7-2A is likely caused by the time necessary for the reaction to produce sufficient fluorescent molecules to register detectable signals.

7.4 Application of our approach

Once the membrane partition is photolyzed, the reactants that were previously separated from each other are allowed to diffuse and react. The time it takes two reactants to encounter each other is determined by the diffusive property and the location of the reactants with respect to the membrane partition, which varies from close to the timescale of membrane photolysis for those immediately adjacent to the membrane area to ~ $r^2/2D$ for those at a distance r away from the lipid membrane where D is the diffusion coefficient of the reactant.[29] The use of vesicles for studying chemical kinetics has been reported previously by Zare and coworkers,[1] in which the small volume of the vesicle is exploited to achieve fast diffusive mixing using electrofusion or electroporation. Here we are concerned with the reaction initiation times that are directly correlated with the thickness of the lipid bilayer and the time scales of membrane breakdown, from which we can extract kinetic information (Figure 7-3B), rather than the time scales of complete mixing of the reactants.

Using this technique, we have studied the deprotonation kinetics of fluorescein, which is one of the most commonly used fluorescent dyes because of its high molar absorptivity, excellent fluorescence quantum yield, its excitability at 488 nm (a readily

available laser wavelength), and good water solubility.[144, 145] In aqueous solution, four forms of fluorescein exist: (i) Cation, (ii) Neutral, (iii) Monoanion, and (iv) Dianion. The fluorescence property of fluorescein varies widely among these different forms and is thus highly pH dependent.[142, 143, 146] Although the equilibrium-state fluorescence properties of fluorescein have been carefully studied,[142, 143, 146] less attention has been paid to its kinetic properties. Here we study the rate of the deprotonation reaction of fluorescein, in which the cationic form (FH^+) is converted to the monoanionic (F^-) and dianionic forms (F^{2-}).

Figure 7-3 demonstrates the capability of using this membrane-breakdown technique to study the rate of deprotonation of fluorescein. To facilitate the interpretation of the rate information obtained from our experiments, we used FEMLAB to create a simplified diffusion-reaction model that simulated our experimental conditions. Figure 3A shows the results of one simulation in which the cationic form of fluorescein was confined to the interior of a 1-μm vesicle (pH < 2), while a basic buffer was present exterior to the vesicle. The color gradient denotes the concentration of the cationic form of fluroescein, with red representing the highest concentration of cationic fluorescein. Prior to photolysis (left panel), cationic fluorescein was distributed homogeneously inside the vesicle. After photolysis of the membrane barrier, the concentration of acidic fluorescein decreased gradually starting at the edge of vesicle, because of the deprotonation of fluorescein as the pH increased (middle and right panel); the diffusion

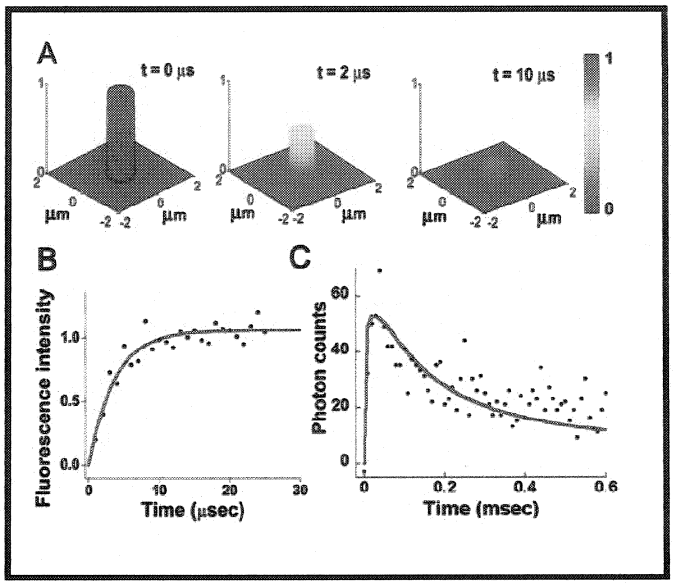

Figure 7-3. **Determination of the kinetics of fluorescein protonation.** (A) Simulation of the fluorescein deprotonation process upon vesicle photolysis, which was carried out in FEMLAB using our reaction-diffusion model; the color gradient represents the concentration of cationic fluorescein at $t = 0$ μs, 2 μs, and 10 μs, respectively. (B) Average experimental data (black dots) and fitting (red line) of the rate of fluorescence increase during the first 30 μs after photolysis of the vesicle membrane at room temperature. Here the vesicle contained ~ 4-μM fluorescein in acidic pH (<2) and 0.1 M sucrose, and the extra-vesicular solution was a phosphate buffer at pH 7.4. The solution that was both inside and outside of the vesicle also contained 0.1 M β-mercaptoethanol. The confocal probe volume was placed at the membrane boundary. (C) Experimental data and fitting showing the deprotonation and diffusion of fluorescein after the photolysis of a 1-μm vesicle. In this experiment, the confocal probe volume was located at the center of the vesicle.

of fluorescein away from the volume previously defined by the vesicle was negligible over this time scale of 10 μs.

The time-dependent diffusion-reaction process is described by eq. (1) below:

$$\frac{\partial}{\partial t}c_i = D\frac{1}{r^2}\frac{\partial}{\partial r}\left(r^2\frac{\partial}{\partial r}c_i\right) + R_i \qquad (1)$$

where D is the diffusion coefficient of fluorescein in water (4.25×10^{-6} cm^2s^{-1}),[32] c and R are the respective concentration and reaction rate of species i. The solution to eq. (1) describes the evolution of fluorescein concentration, c, at position r from the origin at time t. For the reaction of interest, $FH^+ \xrightarrow{-(n+1)H^+} F^{n-}$, eq. (1) is written as a system of differential equations for both reactants and products, respectively:

$$\begin{aligned} \frac{\partial}{\partial t} c_{FH^+} &= D \frac{1}{r^2} \frac{\partial}{\partial r} \left(r^2 \frac{\partial}{\partial r} c_{FH^+} \right) - k c_{FH^+} \\ \frac{\partial}{\partial t} c_{F^{n-}} &= D \frac{1}{r^2} \frac{\partial}{\partial r} \left(r^2 \frac{\partial}{\partial r} c_{F^{n-}} \right) + k c_{FH^+} \end{aligned} \qquad (2)$$

where k is the effective rate constant, and we assume the diffusion coefficient of fluorescein does not change among its different forms (FH^+, F^-, and F^{2-}). The diffusion-reaction equations are subjected to the respective initial conditions (I.C.) and boundary conditions (B.C.), imposed by a vesicle of radius r_v in an infinite medium. At $t = 0$ sec, there is only species FH^+ of concentration C_0 inside the vesicle, and the concentration of F^{n-} is zero everywhere else:

$$\text{I.C.:} \quad \begin{aligned} C_{FH^+}(r \le r_v, t = 0) &= C_o \\ C_{F^{n-}}(r \ge 0, t = 0) &= 0 \end{aligned} \qquad (3)$$

The boundary conditions respectively include a no-flux condition at infinity and a symmetry condition at the origin, as shown in eq. (4).

$$\text{B.C.:}\quad \frac{\partial c_i}{\partial r}(r=\infty, t>0)=0 \qquad \frac{\partial c_i}{\partial r}(r=0, t>0)=0 \qquad (4)$$

To obtain a numerical solution, a boundary r_{max} that is 10,000 times that of r_v is applied to approximate $r = \infty$.

Figure 7-3B and 7-3C shows experimental measurements of the reaction rate of this deprotonation process. In Figure 3B we monitored the rate of fluorescence increase at the membrane boundary of individual vesicles with confocal microscopy, where the cationic fluorescein encounter basic buffer almost instantaneously after the breakdown of lipid membrane. The confocal interrogation probe is ~ 0.5 μm in lateral dimension, and ~ 1 μm along the axial direction. The positioning of the back reflection of the Ar^+ laser focus (confocal spot) onto the membrane boundary (Figure 1) was carried out under high optical magnification (5000×). By fitting the experimental curve recorded for the first 30 μs to a first-order-reaction rate equation ($[F^{n-}] = C_0(1\text{-}e^{-kt})$, where $[F^{n-}]$ is the total concentration of the anionic forms of fluorescein.), we obtained an averaged effective rate constant $k = (2.8 \pm 0.6) \times 10^5\ s^{-1}$ (N = 14). Within the first 30 μs, variations in fluorescence intensity caused by the diffusion of fluorescein in the confocal probe volume were negligible (< 10%).

In Figure 7-3C, we followed over 0.6 ms the fluorescence increase at the center of a 1-μm vesicle, whose size is comparable to the dimension of the confocal probe volume. Here both the reaction and the diffusion of fluorescein were considered, and we fitted our

experimental measurement with our simulation. For the fitting, we calculated the fluorescence intensity from the concentration of fluorescein by integrating the contribution of fluorescence intensity from FH^+, F^-, and F^{2-}, respectively:[26]

$$I = \kappa \sum_i \phi_i \varepsilon_i I_i c_i \qquad (5)$$

where κ is an instrument parameter. ϕ_i, ε_i and I_i are the fluorescence quantum yield, extinction coefficient, and normalized emission of species i at concentration c_i, correspondingly. The respective fluorescence quantum yield and extinction coefficient for FH^+ are 0.18 and 34 $M^{-1}cm^{-1}$, for F^- are 0.37 and 16,425 $M^{-1}cm^{-1}$, and those for F^{2-} are 0.93 and 87,692 $M^{-1}cm^{-1}$, and the pK of the equilibrium between F^{2-} and F^- is 6.43.[142, 146] Under the experimental conditions and given the effective rate constant $k = 2.8 \times 10^5$ s^{-1}, the simulation result matches well the experimental data with an average error of ±21%.

7.5 Conclusion

This chapter describes a new strategy, which is based on the fast breakdown of an ultrathin partition that separates two reactants, to test photolysis efficiency to break down the capsule barrier, and also to achieve a controlled and rapid initiation of chemical reactions (microseconds to milliseconds). The drawback of this method in its current format is the small volume involved, which necessitates a sensitive method of monitoring the chemical reaction, such as confocal fluorescence detection. The advantages of this

method are its general applicability, and the well-defined and fast reaction initiation times that can be achieved, which bridges nicely the faster time scales that are accessible mostly with laser-based triggering experiments (picoseconds to nanoseconds) and the slower time scales that are studied most frequently with flow-based devices (milliseconds to seconds).

Chapter 8 Single Cell Signaling

8.1 Introduction

Cells respond to their environment through a complex and interdependent series of signal transduction pathways that frequently begin at the cell membrane with high spatial and temporal resolutions (e.g. exocytosis, endocytosis, synaptic transmission). [147] This plasma membrane defines the boundary of the cell, encloses the cytosol, and maintains the intracellular environment. The cell membrane not only acts as a barrier that protects the cell from the extracellular space, but with its embedded receptors, surface-anchored proteins and signaling molecules serves also as a sensor and communicator to the extracellular world.[148] Although a typical mammalian cell measures only ten to twenty micrometers in diameter, the cell is a highly organized and spatially heterogeneous structure. To study and dissect the mechanism and signaling pathways by which a single cell processes the arrival of a particular signal at its membrane surface, we have developed a technique by which a precisely timed stimulus can be delivered to the cell with high spatial resolution.

To evoke a ligand-induced response from a cell, most experiments have relied either on the perfusion of the cell in a microchamber[149, 150] or with pressure microinjection, [151, 152] or on iontophoresis, [153, 154] or on the flash photolysis of a caged compound. [155-158] Although the implementation of perfusion and iontophoresis are straightforward and their strategy are generally applicable, these approaches typically lack both high spatial and temporal resolution. [152, 153] UV photolysis of a caged compound, in combination with two-photon excitation, [2, 159, 160] can overcome many of

the spatial and temporal limitations of perfusion and iontophoresis. The spatial resolution of two-photon excitation is typically on the order of several hundred nanometers, defined mostly by the tightness of the laser focus. [2, 159] The temporal resolution of two-photon uncaging varies, and is limited by the timescale of the photochemical steps by which the photolysis of the caging group occurs, which is typically in the tens of microseconds to milliseconds range. [161, 162] Despite the good spatial and temporal resolution that can be achieved by using two-photon photolysis of a caged molecule, the use of caged compound suffers from a number of drawbacks: (1) The design and synthesis of a suitable caged molecule are complex and time consuming, (2) The caging of large bioactive molecules such as peptides (e.g. cytokines) and proteins is difficult if at all possible, and (3) The uncaging of multiple stimuli simultaneously is often cumbersome.

8.2 New strategy

This chapter describes a new strategy for delivering defined packages of stimuli to single cells with both high spatial and temporal resolutions. Figure 8-1A schematically depicts our approach. Optical trapping is used to manipulate individual vesicles (or any suitable nanocontainers) that encapsulate the bioactive molecules of interest. Once a select vesicle is placed adjacent to the target cell, a single 4-ns pulse from a UV laser (337 nm), which is aligned collinear with the trapping laser (1064 nm), is used to photolyze the optically trapped vesicle and to release the encapsulated molecules. Pulsed UV laser can provide short wavelength light with high instantaneous power, and is

widely used in photoablating biotissues and polymers. [163] Figure 8-1B shows the positioning and trapping of a single 0.1-μm (in diameter) vesicle, which was formed by extrusion, in contact with a CHO-M1 cell.

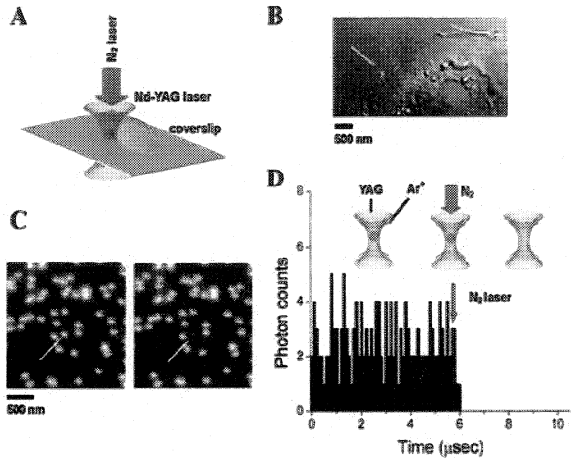

Figure 8-1. **Spatial and temporal characterization of our strategy.** (A) Schematic illustration of the relative positions of the YAG laser (red; 1064 nm; ~ 0.3 W prior to entering the N.A. 1.3 oil immersion objective), the trapped vesicle (blue), the target cell (green), and the N_2 laser (purple; 337 nm; ~ 3 μJ prior to entering the objective). (B) Fluorescence-Normaski image showing the precise positioning of a single 0.1-μm DiO-C18 stained vesicle adjacent to a CHO-M1 cell. (C) Demonstration of the spatial resolution of the focused N_2 laser in which a single 0.11-μm fluorescent beads (arrow) was photolyzed by a single 4-ns N_2 laser pulse. (D) Demonstration of the temporal resolution of single-vesicle photolysis, in which the vesicle was photolyzed within 0.3 μs; the inset depicts schematically the sequence of steps.

Figure 8-1C demonstrates the selective photolysis of a single 0.11 μm fluorescent polystyrene bead that was in close proximity (less than 0.2 μm) to another 0.11 μm bead. In contrast to the use of caged compounds in which the photolysis volume and thus the

spatial resolution is determined by the excitation focal volume, the photolysis volume in our approach is defined by the size of the vesicle and by the ability to optically trap and precisely position such small vesicles. In principal, by using small nanocontainers (e.g. less than 0.1 μm), the photolysis volume can be significantly smaller than the laser excitation volume defined by the tight focus. It is also possible to spectrally select the vesicle to be photolyzed by doping the vesicle membrane with absorptive dyes that are tuned to the photolysis wavelength. [164]

Figure 8-1 D illustrates the time scale of photolyzing a single vesicle; the inset schematically illustrates the experiment. A single 1-μm vesicle, which was stained with a membrane dye (DiO-C18), was first optically trapped in solution. The fluorescence signal from the trapped vesicle was continuously monitored with a confocal detection system in which the laser focus of the Ar^+ laser (488 nm) was aligned collinear with the trapping laser. At 5.0 μs, a trigger was sent from the computer to initiate the firing of a single 4-ns pulse from the N_2 laser, which was aligned collinear with both the trapping laser and Ar^+ laser. The arrival of the N_2 laser pulse onto the trapped vesicle (arrow), which was measured to occur at 0.7 μs after triggering, caused the photolysis of the vesicle and the disappearance of the fluorescence signal. Photolysis of a single vesicle occurs within 0.3 μs, which is significantly shorter than the uncaging times of most caged molecules.

8.3 Prove of the concept

Vesicle delivery. To demonstrate the applicability of this approach for the spatially resolved delivery of stimuli to single cells, we encapsulated carbachol into the vesicle interior. Carbachol binds to the muscarinic acetylcholine receptors,[165] activates G-protein that hydrolizes phosphoinositide to produce IP_3, which then causes the increase of the intracellular levels of calcium.[166] We visualized this increase with the fluorescent calcium indicator, fluo-3. Figure 7-2 shows the activation of a fluo-3 loaded CHO-M1 cell that has been transfected to express muscarinic acetylcholine receptors (CHO-M1-WT3, ATCC).

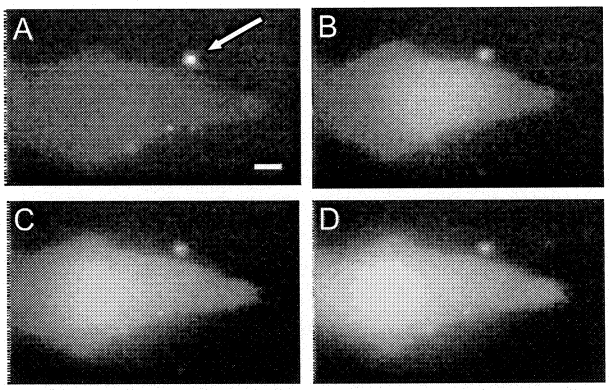

Figure 8-2. **Response of a fluo-3 loaded CHO-M1 cell to carbachol, which was released from the photolysis of a single 0.6 μm vesicle.** (A) Image of the vesicle and the cell before vesicle (arrow) photolysis. (B)-(D) Sequential fluorescent images showing the increase of the intracellular calcium level after vesicle photolysis. The time interval between A and B is 1 sec, while the time intervals from B to C and from C to D are 0.15 sec, and 0.55 sec, respectively. The vesicle was formed in HEPES buffer (pH 7.4) containing 0.1 M carbachol, and was doped with cholesteryl 1-pyrenebutyrate and DiO-C18 at 50 mol % and 1 mol %, respectively. The scale bar represents 1 μm.

A single 0.6-μm vesicle was positioned with optical trapping at ~ 0.5 μm from the CHO-M1 cell. To visualize the small vesicle, we stained the vesicle membrane with 1% DiO-C18. The photolysis of the vesicle resulted in the release of the intra-vesicular carbachol and the collapse of the residual vesicle membrane onto the surface of the coverslip. The released carbachol caused the localized increase of intracellular calcium, which propagated throughout the entire cell (Fig 8-2(B-D)). The amount of stimuli to be delivered to the cell can be varied easily by controlling either the size of the vesicle or the concentration of the stimuli during their encapsulation into the vesicle.[46] In contrast to the use of caged compounds, all biologically active molecules are confined to the vesicular interior, thus avoiding any undesirable side effects that may be caused by the presence of caged or partially uncaged molecules in contact with cells.[167] Therefore, our technique is based on the physical separation of the stimuli from cells, rather than relying on "chemical" separation as is the case for caged compounds.

Nanoparticle delivery. To illustrate the use of nanocapsules for studying single cells, we loaded the capsule with carbachol, an agonist to the muscarinic acetylcholine receptor type 1 (M1) and studied the calcium signaling in Chinese Hamster Ovary cells (CHO) transfected with M1 receptors. Figure 8-3A shows our experimental procedure, in which a single capsule loaded with carbachol was optically trapped and positioned adjacent to a single cell (CHO M1) (left panel) followed by application of a single N_2 laser pulse to release the encapsulated carbachol (right panel). The binding of carbachol by the receptor initiates a calcium-signaling cascade, which ultimately results in the

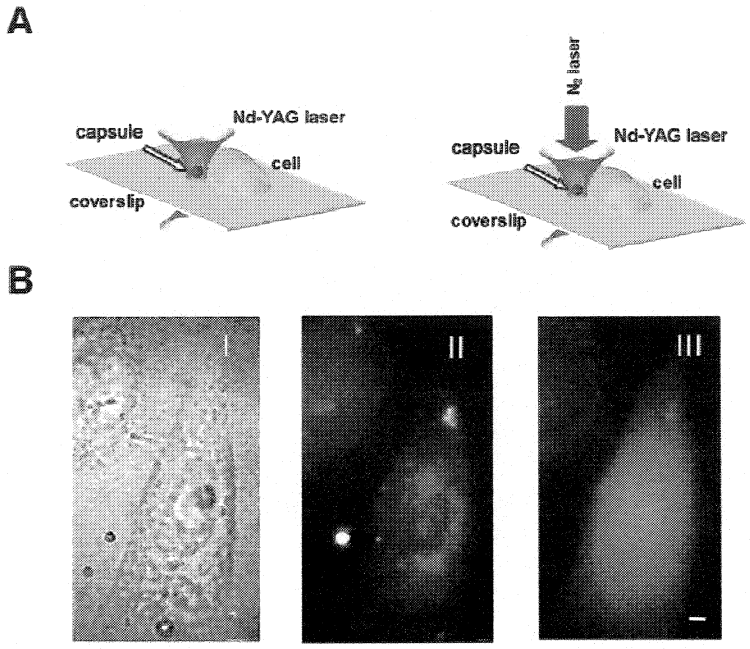

Figure 8-3. **Response of a fluo-3 loaded CHO-M1 cell to the local release of carbachol from a polystyrene-based capsule. (A)** Schematic illustration of the experimental design. **(B-I & B-II)** Bright-field **(B-I)** and fluorescence **(B-II)** images of the capsule and cell before the photolysis of the capsule, which was loaded with fluorescein (in addition to carbachol) for ease of visualization; **(B-III)** Increase in intracellular concentration of calcium visualized by fluo-3 after photolysis of the capsule and release of carbachol.

increase of intracellular calcium, a process that we monitored with the calcium indicator, fluo-3.[9] Figure 8-3B-I and 8-3B-II shows the bright-field and fluorescent images of the capsule and the cell prior to release of carbachol, respectively, and Figure 8-3B-III shows the resultant increase of intracellular concentrations of calcium upon activation by carbachol. We have consistently observed that the amount of carbachol present within the capsule is more than sufficient to trigger a cellular response.

8.4 Conclusion

The main drawback of our approach lies in the finite size of the vesicles, which may make them unsuitable for intracellular applications. Although methods exist for introducing small nanoparticles into single cells, [168, 169] the intracellular diffusion of these nanoparticles may be restricted. For the introduction of extracellular stimuli, however, this method possesses a number of advantages: (1) Any membrane impermeable molecules, including peptides and proteins, can be encapsulated into vesicles (or other nanocontainers) and be delivered to cells, (2) It is straightforward to deliver multiple stimuli, with each stimulus present at a given concentration, to single cells simultaneously, (3) All stimuli are confined to the vesicle interior and are physically and spatially separated from the cells, and (4) It is possible to spectrally tuned the photolysis wavelength by doping the vesicle membrane with the appropriate absorptive dyes. The strategy we described is not limited to vesicles, but to any nanocontainers of choice. For quantitative applications in which the amount of stimuli delivered must be controlled, the size of the extruded vesicle must be uniform, which can be achieved by purifying the vesicles with respect to size using methods of separation. Alternatively, monodispersed non-vesicle based nanocontainers may be designed and synthesized. This technique offers new possibilities in the study of the heterogeneous organization of single cells and the probing of the dynamics of cellular responses after a precisely timed delivery of stimuli.

Chapter 9 Mapping the cell surface receptors

9.1 Introduction

Cell membrane receptors and proteins receive extracellular stimulations and transform them into intracellular signals. [170, 171] The distribution of receptors and proteins on the cell membrane determines and affects the rate and pattern of the propagation of these intracellular signals. [171-176] Previous studies indicate membrane proteins are often expressed in different morphological regions of the plasma membrane, and within a local area, the proteins tend to form clusters and patches, rather than distributed homogenously and continuously on the membrane. [176, 177] This confinement and localization of proteins is on a length scale of tens of nanometers to a few micrometers.

Although a number of high-resolution imaging approaches are available for visualizing the spatial distribution of proteins and receptors on the cell membrane, [170, 178, 179] these methods do not provide functional information with regard to the activities of these proteins. Techniques capable of probing the functions of membrane proteins with high spatial and temporal resolution are limited, and much effort has been spent to develop such capabilities. [172, 180] The most notable and promising of these methods is the two-photon photolysis of caged molecules. [181-183] As we analyzed in chapter 1, caged compounds suffer a series of inherited drawbacks such as troublesome synthesis procedure, biocompatibility etc, and these requirements place significant constraints and design challenges on the development of good caged compounds, and often limit them to small molecules rather than peptides and proteins. [8, 9]

To overcome the disadvantages of utilizing caged compounds, while retaining the high spatial resolution characteristic of two-photon photolysis, this paper describes the development of a technique that uses nanocontainers, particularly lipid vesicles, to physically confine the biostimuli of interest, optical trapping to position the nanocontainers in close proximity to the cellular structure under study, and UV photolysis to release the encapsulated molecules onto the cell. We demonstrate the feasibility of this strategy by applying it to the study of calcium signaling, in which the localized activation of muscarinic acetylcholine receptors is triggered by carbachol that is released from a single vesicle.

9.2 Technique characterization and receptor mapping

Characterization of lipid vesicles as delivery vessels: In comparison with caged compounds, one key feature of our approach is the use of vesicles as nanocontainers to physically separate the molecules of interest from their cellular targets, rather than rendering the molecules biologically inactive with chemical groups. Nanocontainers can act as versatile delivery vessels of cellular stimuli because of the diverse synthetic methods by which nanocontainers with desired material properties and physical dimensions and shapes can be produced. [184, 185] Lipid vesicles in particular are easily formed in aqueous solution via self assembly and their sizes can be tuned over a wide range from tens of nanometers to many micrometers. [186] In contrast to two-photon

uncaging, the volume from which the stimuli is released is defined by the size of the vesicle rather than by the focal volume of the photolysis laser. By using vesicles that are tens of nanometers in diameter and provided one can position the vesicle with similar accuracy, the location from which stimuli is released can be exquisitely controlled.

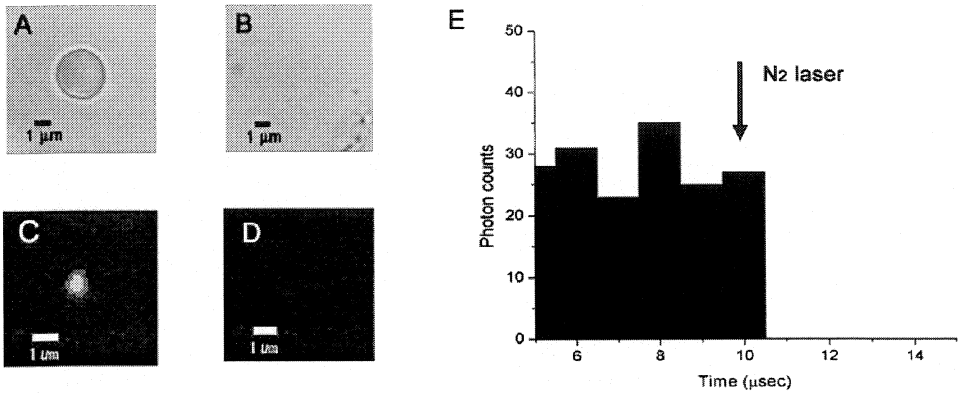

Figure 9-1. **Demonstration of vesicle photolysis upon irradiation with a single 3ns laser pulse at 337nm.** (A, B) Bright-field CCD camera images showing before (A) and after (B) the photolysis of a ~ 3µm-diameter vesicle. (C, D) Fluorescent images showing before (C) and after (D) the photolysis of a small 600nm-diameter vesicle. (E) Fluorescence signal trace showing the time scale of the photolysis of an optically trapped 600nm-diameter vesicle. The arrow marked the firing of the N_2 laser pulse. The DPPC vesicles were doped with cholesteryl 1-pyrenebutyrate and DiO-C18 at 50 and 1 mol %, respectively.

Using sonication, extrusion, or rotary evaporation, we are able to produce vesicles that range in size from 50nm to 50µm. The method that we use most often is extrusion, which can generate vesicles with diameters that can be controlled from 100nm to 600nm. These vesicles are small enough for the localized stimulation of single cells, yet large enough for facile manipulation with optical trapping. Figure 9-1(A & C) are bright field and fluorescence images showing a giant vesicle (~ 3 µm in diameter) produced with

rotary evaporation and a large vesicle (~ 600nm in diameter) generated by extrusion, respectively. Although we can produce small vesicles easily with sonication and manipulate them with optical trapping, these vesicles tend to be more difficult to visualize and trap for prolonged periods of time (minutes) with our current optical setup. In comparison with the synthesis of caged molecules, the preparation of lipid vesicles can be carried out routinely and easily. The drawback in the use of vesicles lies in the lack of quantitative control over the amount of stimuli released. Because there is a distribution in the sizes of the vesicles formed, depending on the particular method of preparation, the intravesicular volume and thus the number of contained molecules will vary with the size of the vesicle. This drawback may be overcome, however, by additional purification and separation of the vesicles or with the use of non-vesicle based monodispersed nanocontainers.

For lipid vesicles to be used as delivery vessels, the vesicular contents must be released controllably and with high yield. Figures 9-1 & 9-2 demonstrate and characterize the photo-destruction of the lipid membrane barrier and the concurrent release of the encapsulated molecules. We used a single 3ns pulse at 337nm from a N_2 laser to photolyze the lipid membrane. To increase the ease and yield of photolysis, the membrane was doped with a dye (cholesteryl 1-pyrenebutyrate at 50 mol%) that has high absorption cross-section in the UV. The exact mechanism by which the integrity of the lipid membrane was compromised is unclear, but is likely caused by a combination of photochemical and photothermal processes. [163]

Figure 9-1A & 9-1B shows the photolysis of a 3μm-diameter vesicle. For vesicles with diameters in the micrometer range, high laser power (~ 2 μJ prior to entering the objective) is required. These vesicles always leave membrane residues on the coverslip (Fig. 9-1B) if the photolysis occurred near (within a few micrometers) the surface of the coverslip. In addition, because the diameter of the photolysis laser beam at the focal plane (~ hundreds of nanometers) is smaller than that of the vesicle, the vesicle sometimes tends to "fragment" to form smaller vesicles. For vesicles that are a few hundred nanometers in diameter, laser powers of less than 1 μJ are typically sufficient for photolysis. These nanometer-sized vesicles can be photolyzed completely without visible remnants (Fig. 9-1C & 9-1D). Figure 3E characterizes the time scale of photolysis, in which the fluorescence signal from a membrane dye (DiO-C18) was monitored continuously with confocal microscropy as the trapped vesicle was being photolyzed. Here, the three laser beams (488nm from the Ar^+, 1064nm from the YAG, and 337nm from the N_2) were aligned co-linearly prior to entering the objective of the microscope. The photo-destruction of the membrane occurs in the sub-microsecond time scale (Fig. 9-1E).

Figure 9-2 shows the encapsulation in and release of a fluorescent dye, 5-carboxyrhodamine 6G, from a trapped 600nm vesicle. The high quantum yield and photostability of this dye makes it suitable for visualization of this release process under fluorescence imaging. [187] Most water-soluble proteins, peptides, nucleic acids, and small molecules can be easily encapsulated into the vesicles without modification of the

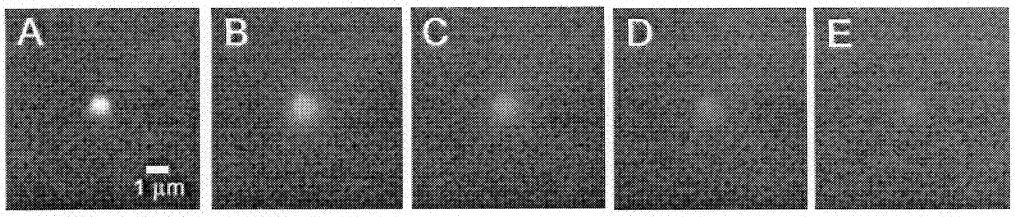

Figure 9-2. **A sequence of fluorescence images showing the photolysis of a single optically trapped 600nm-diameter vesicle that contained 5-carboxyrhodamine 6G in a PBS buffer solution.** (A) is the fluorescent image before photolysis while (B-E) are the subsequent images immediately after the firing of the N_2 laser. The time interval between each adjacent image is 33 ms.

vesicle preparation procedure. The use of sub-micrometer diameter vesicles offers good spatial control and resolution for locally stimulating the cell, while micrometer-sized vesicles are useful when the amount of stimuli needed is high. The ease with which loaded vesicles of defined sizes can be prepared makes this technique a versatile and powerful platform for carrying out spatially resolved functional studies of single cells.

Functional study of cellular response upon vesicular release of stimulus: To demonstrate the concept of our approach, we studied the functional response of CHO cells transfected with muscarinic acetylcholine type 1 receptor upon localized stimulation by carbachol, an agonist to the receptor. Carbachol causes increase of the intracellular levels of calcium via inositol 1,4,5-triphosphates (IP_3). [148] We used the calcium indicator, fluo-3, to monitor the intracellular concentration of calcium. Figure 6-3 shows this calcium signaling event, in which a single 600nm vesicle loaded with carbachol was trapped and positioned adjacent to the CHO-M1 cell followed by photolysis of the vesicle with a single 3ns laser pulse (Fig. 9-3A). Upon photolysis and vesicular release of

carbachol, the intracellular levels of calcium raised markedly as visualized by the increase in fluorescence intensity of fluo-3 (Fig. 9-3B). The fluorescence images of the cells in Fig. 9-3A & 9-3B appear blurry in part because we positioned the vesicle slightly above the cell in this particular experiment so the cell was slightly out of focus.

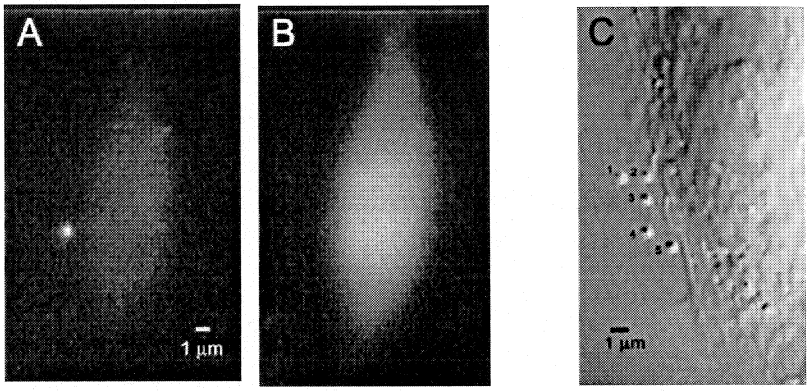

Figure 9-3. The possibility to map the receptors on cell membrane. (A,B) Response of a CHO-M1 cell to the localized delivery of carbachol from a 600nm-diameter vesicle. The CHO-M1 cell was loaded with fluo-3 and the vesicle contained 0.1 M carbachol. (C) Optical manipulation and positioning of a 600nm-diameter vesicle along the periphery of a CHO-M1 cell as imaged under Normaski; the vesicle was moved sequentially from location 1 through 5.

Figure 9-3C shows a CHO-M1 cell under Normaski in which the morphology and the different processes of the cell can be clearly distinguished. To illustrate the spatial control offered by this method for mapping the functional distribution of cell surface proteins, we optically trapped a single 600nm vesicle and positioned it along the different processes of the CHO-M1 cell. Unlike the use of caged compounds where the cell must be perfused with significant concentrations of the compound, which may adversely affect cellular physiology owing to both the presence of impurities and small amounts of

uncaged molecules, [167] this method permits the positioning of a single nanometer-sized vessel in close proximity to the cell with great spatial control. Here the cell is free of exposure to non-biological organic caged compounds with a spatial localization of stimuli release that is comparable to two-photon uncaging.

9.3 Conclusions

The use of nanocontainers, which in our case are lipid vesicles with tailored compositions and sizes, overcomes the synthetic challenges associated with the use of caged compounds and provides a versatile platform for "caging" any membrane-impermeable molecules of interest. We believe this approach offers new versatilities for studying the heterogeneous organization of cells and for unraveling the dynamics of signaling mechanisms and cellular responses. The main drawbacks of this approach in its current form are: (1) The preclusion of most intracellular applications due to the physical dimension of the vesicles, (2) The lack of quantitative control over the amount of stimuli released from the vesicle owing to variations in the sizes of the vesicles, and (3) The limited shelf-life of vesicles (hours to days), which necessitates the periodic preparation of new vesicles. These latter two constraints, however, may be overcome with the use of non-vesicle based monodispersed nanocontainers, such as hollow polystyrene beads.

Bibliography

(1) Simons, K.; Ikonen, E. *Nature* **1997**, *387*, 569-572.
(2) Shear, J. B. *Analytical Chemistry* **1999**, *71*, 569A-642A.
(3) Anderson, R. G.; Jacobson, K. *Science* **2002**, *296*, 1821-1825.
(4) Rothberg, K. G.; Heuser, J. E.; Donzell, W. C.; Ying, Y. S.; Glenney, J. R.; Anderson, R. G. *Cell* **1992**, *68*, 673-682.
(5) Goppert-Mayer, M. *Ann. Phys. (Leipzig)* **1931**, *9*, 273.
(6) Denk, W.; Strickler, J. H.; Webb, W. W. *Science* **1990**, *248*, 73.
(7) Sheppard, C. J. R.; Kompfner, R. *Appl. Opt.* **1978**, *17*, 2879.
(8) Morgan, C. G.; Bisby, R. H.; Johnson, S. A.; Mitchell, A. C. *FEBS Letters* **1995**, *375*, 113-116.
(9) Sun, B.; Chiu, D. T. *J. Am. Chem. Soc.* **2003**, *125*, 3702-3703.
(10) Ashkin, A. *Phys. Rev. Lett.* **1970**, *24*, 156-159.
(11) Minsky, M.: U.S., 1957.
(12) Davidovits, P.; Egger, M. D. *Appl. Opt.* **1971**, *10*, 1615-1619.
(13) Egger, M. D. *Trends Neurosci.* **1989**, *12*, 11.
(14) Alecio, M. R.; Golan, D. E.; Veatch, W. R.; Rando., R. R. *Proc. Natl. Acad. Sci. USA* **1982**, *79*, 5171-5174.
(15) Gregoriadis, G.; Florence, A. T.; Patel, H. M. *Liposomes in drug delivery*; T&F STM: London, 1993.
(16) Gregoriadis, G. *Liposomes as drug carriers: recent trends and progress*; John Wiley & Sons Inc.: New York, 1988.
(17) Mezei, E.; Meisner, D. *Liposomes and nanoparticles as ocular drug delivery systems*; CRC press: Boca Raton, 1993.
(18) Allen, T. M.; Cullis, P. R. *Science* **2004**, *303*, 1818-1822.
(19) Langer, R. *Nature* **1998**, *392*, 5-10.
(20) Kmiec, E. B. *Gene Therapy* **1999**, *6*, 1-3.
(21) Simons, K.; Vaz, W. L. C. *Annu. Rev. Biophys. Biomol. Struct.* **2004**, *33*, 269-295.
(22) Veatch, S. L.; Keller, S. L. *Biophys. J.* **2003**, *85*, 3074-3083.
(23) Edidin, M. *Trends in Cell Biology* **2001**, *11*, 492-496.
(24) Chiu, D. T.; Wilson, C. F.; Ryttsen, F.; Stromberg, A.; Farre, C.; Karlsson, A.; Nordholm, S.; Gaggar, A.; Modi, B. P.; Moscho, A.; Garza-Lopez, R. A.; Orwar, O.; Zare, R. N. *Science* **1999**, *283*, 1892-1895.
(25) Cans, A.-S.; Wittenberg, N.; Karlsson, R.; Sombers, L.; Karlsson, M.; Orwar, O.; Ewing, A. *Proc. Natl. Acad. Sci. USA* **2003**, *100*, 400-404.
(26) Karlsson, M.; Davidson, M.; Karlsson, R.; Karlsson, A.; Bergenholtz, J.; Konkoli, Z.; Jesorka, A.; Lobovkina, T.; Hurtig, J.; Voinova, M.; Orwar, O. *Annual Review of Physical Chemistry* **2004**, *55*, 613-649.
(27) Kulin, S.; Kishore, R.; Helmerson, K.; Locascio, L. *Langmuir* **2003**, *19*, 8206-8210.

(28) Messersmith, P. B.; Vallabhaneni, S.; Nguyen, V. *Chem. Mater.* **1998**, *10*, 109-116.
(29) Bolinger, P.-V.; Stamou, D.; Vogel, H. *J. Am. Chem. Soc.* **2004**, *126*, 8594-8595.
(30) Sun, B.; Lim, D. S. W.; Kuo, J. S.; Kuyper, C. L.; Chiu, D. T. *Langmuir* **2004**, *20*, 9437-9440.
(31) de la Maza, A.; Marsal, A.; Cot, J.; Parra, J. L. *J. Am. Leather Chemists Association* **1994**, *89*, 123-131.
(32) de la Maza, A.; Manich, A. M.; Coderch, L.; Parra, J. L. *Textile Res. J.* **1995**, *65*, 163-170.
(33) Arshady, R.; Pouliquen, D.; Halbreich, A.; Roger, J.; Pons, J.-N.; Bacri, J.-C.; Da, S.; Maria, D. F.; Hafeli, U. *Microspheres, Microcapsules & Liposomes* **2002**, *5 (Dendrimers, Assemblies, Nanocomposites)*, 283-329.
(34) Perkins, W. R.; Minchey, S. R.; Ahl, P. L.; Janoff, A. S. *Chem. Phys. Lipids* **1993**, *64*, 197-217.
(35) Betageri, G. V.; Parsons, D. L. *Int. J. Pharm.* **1992**, *81*, 235-241.
(36) Fresta, M.; Villari, A.; Puglisi, G.; Cavallaro, G. *Int. J. Pharm.* **1993**, *99*, 145-156.
(37) Bangham, A. D., Standish, M. M. and Watkins, J. C. *J. Mol. Biol.* **1965**, *13*, 238.
(38) Bangham, A. D. *Prog. Biophys. Mol. Biol.* **1968**, *18*, 31.
(39) Huang, C. *Biochemistry* **1969**, *8*, 344.
(40) Moscho, A.; Orwar, O.; Chiu, D. T.; Modi, B. P.; Zare, R. N. *Proc. Natl. Acad. Sci. USA* **1996**, *93*, 11443-11447.
(41) Akashi, K.; Miyata, H.; Itoh, H.; Kinosita, K. J. *Biophys. J.* **1998**, *74*, 2973-2982.
(42) Akashi, K.; Miyata, H.; Itoh, H.; Kinosita, K. J. *Biophys. J.* **1996**, *71*, 3242-3250.
(43) Marsh, D. *CRC handbook of lipid bilayers*; CRC Press: Boca Raton, Ann Arbor, Boston, 1990.
(44) Nicholas, A. R.; Scott, M. J.; Kennedy, N. I.; Jones, M. N. *Biochim. Biophys. Acta* **2000**, *1463*, 167-178.
(45) Kulkarni, S. B.; Betageri, G. V.; Singh, M. *J. Microencapsulation* **1995**, *12*, 229-246.
(46) Walde, P.; Ichikawa, S. *Biolomecular Engineering* **2001**, *18*, 143-177.
(47) Elorza, B.; Elorza, M. A.; Sainz, M. C.; Chantres, J. R. *J. Microencapsulation* **1993**, *10*, 237-248.
(48) Sun, B.; Chiu, D. T. *Proceedings of SPIE-The International Society for Optical Engineering* **2003**, *5222*, 118-125.
(49) Sun, B.; Chiu, D. T. *Langmuir* **2004**, *20*, 4614-4620.
(50) Crank, J. *The mathematics of diffusion*, 2nd ed.; Clarendon press: Oxford, 1975.
(51) Culbertson, C. T.; Jacobson, S. C.; Ramsey, J. M. *Talanta* **2002**, *56*, 365-373.
(52) Baumgart, T.; Hess, S. T.; Webb, W. W. *Nature* **2003**, *425*, 821-824.
(53) Veatch, S. L.; Keller, S. L. *Phys. Rev. Lett.* **2002**, *89*, 268101.
(54) Dietrich, C.; Bagatolli, L. A.; Volovyk, Z. N.; Thompson, N. L.; Levi, M.; Jacobson, K.; Gratton, E. *Biophys. J.* **2001**, *80*, 1417-1428.
(55) Evans, E.; Metcalfe, M. *Biophys. J.* **1984**, *46*, 423-426.
(56) Vuillemard, J. C. *J. Microencapsulation* **1991**, *8*, 547-562.

(57) Wagner, A.; Vorauer-Uhl, K.; Kreismayr, G.; Katinger, H. *J. Liposome Res.* **2002**, *12*, 271-283.
(58) Puglisi, G.; Fresta, M.; La Rosa, C.; Ventura, C. A.; Panico, A. M.; Mazzone, G. *Pharmazie* **1992**, *47*, 211-215.
(59) Benita, S.; Poly, P. A.; Puisieux, F.; Delattre, J. *J. Pharm. Sci.* **1984**, *73*, 1751-1755.
(60) Szoka, F. C.; Parahadjopoulos, D. *Annu. Rev. Biophys. Bioeng.* **1980**, *9*, 467-508.
(61) Molpeceres, J.; Aberturas, M. R.; Guzman, M. *J. Microencapsulation* **2000**, *17*, 599-614.
(62) Grier, D. G. *Nature* **2003**, *424*, 810-816.
(63) Meier, W. *Chem. Soc. Rev.* **2000**, *29*, 295-303.
(64) Discher, D. E.; Eisenberg, A. *Science* **2002**, *297*, 967-973.
(65) McDonald, C. J.; Devon, M. J. *Adv. Colloid Interface Sci.* **2002**, *99*, 181-213.
(66) Silvert, P.-Y.; Herrera-Urbina, R.; Duvauchelle, N.; Vijayakrishnan, V.; Elhsissen, K. T. *J. Mater. Chem.* **1996**, *6*, 573-577.
(67) Silvert, P.-Y., Herrera-Urbina, R., Elhsissen, K. T. *J. Mater. Chem.* **1997**, *7*, 293-299.
(68) Ducamp-Sanguesa, C.; Herrera-Urbina, R.; Figlarz, M. *J. Solid State Chem.* **1992**, *100*, 272-280.
(69) Sun, Y.; Gates, B.; Mayers, B.; Xia, Y. *Nano Letters* **2002**, *2*, 165-168.
(70) Fievet, F.; Lagier, J. P.; Blin, B.; Beaudoin, B.; Figlarz, M. *Solid State Ionics* **1989**, *198*, 32-33.
(71) Giersig, M.; Ung, T.; Liz-Marzan, L. M.; Mulvaney, P. *Adv. Mater.* **1997**, *9*, 570.
(72) Yin, Y.; Lu, Y.; Sun, Y.; Xia, Y. *Nano Lett.* **2002**, *2*, 427-430.
(73) Hardikar, V. V.; Matijevic, E. *J. Colloid Interface Sci.* **2000**, *221*, 133-136.
(74) Stober, W.; Fink, A.; Bohn, E. *J. Colloid Interface Sci.* **1968**, *26*, 62-69.
(75) Han, M.; Gao, X.; Su, J. Z.; Nie, S. *Nature Biotechnol.* **2001**, *19*, 631-635.
(76) Walter, B. *Ann, Phys. (Leipzig)* **1888**, *34*, 316-326.
(77) Chen, R. F.; Knutson, J. R. *Anal. Biochem.* **1988**, *172*, 61-77.
(78) McDonald, C. J.; Devon, M. J. *Advances in Colloid and Interface Science* **2002**, *99*, 181-213.
(79) Choi, S.-W.; Kim, W.-S.; Kim, J.-H. *J. dispersion sci. technology* **2003**, *24*, 475-487.
(80) Kiser, P. F.; Wilson, G.; Needham, D. *J. Controlled Release* **2000**, *68*, 9-22.
(81) van der Schee, H. A.; Lyklema, J. *The effect of polymers on dispersion properties*; Academic press: London, 1982.
(82) Mulvaney, P.; Liz-Marzan, L. M.; Giersig, M.; Ung, T. *J. Mater. Chem.* **2000**, *10*, 1259-1270.
(83) Jones, G. D. *Polyelectrolytes*; Technomic: Westerport, CT, 1976.
(84) Claesson, P. M.; Dahlgren, M. A. G.; Eriksson, L. *Colloids surfaces A: Physiocochem. Eng. Aspects.* **1994**, *93*, 293.
(85) Evers, O. A.; Fleer, G. J.; Scheutjens, J. M. H. M.; Lyklema, J. *J. Colloid Interface Sci.* **1986**, *111*, 504.
(86) Hesselink, F. T. *J. Colloid Interface Sci.* **1977**, *60*, 448.

(87) Beach, E. R.; Tormoen, G. W.; Drelich, J.; Han, R. *J. Controlled Release* **2002**, *247*, 84-99.
(88) Huang, H.; Leobandung, W.; Foss, A.; Peppas, N. A. *J. Controlled Release* **2000**, *65*, 63-71.
(89) Eriksson, B.; Hardin, A.-M. *Flocculation in biotechnology and separation systems*; Elsevier Science Publishers B.: Amsterdam, 1987.
(90) Fleer, G. J.; Cohen Stuart, M. A.; Scheutjens, J. M. H. M.; Cosgrove, T.; Vincent, B. *Polymers at interfaces*; Chapman & Hall: London, 1993.
(91) Poptoshev, E.; Rutland, M. W.; Claesson, P. M. *Langmuir* **1999**, *15*, 7789-7794.
(92) Poptoshev, E.; Rutland, M. W.; Claesson, P. M. *Langmuir* **2000**, *16*, 1987-1992.
(93) Blomberg, E.; Poptoshev, E.; Claesson, P. M.; Caruso, F. *Langmuir* **2004**, *20*, 5432-5438.
(94) Caruso, F.; Lichtechfeld, H.; Donath, E.; Mohwald, H. *Macromolecules* **1999**, *32*, 2317-2328.
(95) Sauer, M.; Meier, W. *Chem. Commun.* **2001**, 55-56.
(96) Sauer, M.; Streich, D.; Meier, W. *Adv. Mater.* **2001**, *13*, 1649-1651.
(97) Farhat, T. R.; Schlenoff, J. B. *Langmuir* **2001**, *17*, 1184-1192.
(98) Moya, S.; Donath, E.; Sukhorukov, G. B.; Auch, M.; Baumler, H.; Lichtechfeld, H.; Mohwald, H. *Macromolecules* **2000**, 4538-4544.
(99) Antipov, A. A.; Sukhorukov, G. B.; Donath, E.; Mohwald, H. *J. Phys. Chem. B* **2001**, *105*, 2281-2284.
(100) Antipov, A. A.; Sukhorukov, G. B.; Donath, E.; Mohwald, H. *Langmuir* **2003**, *19*, 2444-2448.
(101) Georgieva, R.; Moya, S.; Hin, M.; Mitlohner, R.; Donath, E.; Kiesewetter, H.; Mohwald, H.; Baumler, H. *Biomacromolecules* **2002**, *3*, 517-524.
(102) Sukhorukov, G. B.; Donath, E.; Davis, S. A.; Lichtechfeld, H.; Caruso, F.; Popov, V. I.; Mohwald, H. *Polym. Adv. Technol.* **1998**, *9*, 759-767.
(103) O'Regan, B.; Gratzel, M. *Nature* **1991**, *353*, 737.
(104) Bedja, I.; Hotchandi, S.; Kamat, P. V. *J. Phys. Chem.* **1993**, *97*, 11064.
(105) Colvin, V.; Schlamp, M.; Alivisatos, A. P. *Nature* **1994**, *370*, 354.
(106) Neeves, A. E.; Birnboim, M. H. *J. Opt. Soc. Am. B* **1989**, *6*, 787.
(107) Micheletto, R.; Fukuda, H.; Ohtsu, M. *Langmuir* **1995**, *11*, 3333.
(108) Kim, S. S.; Zhang, W.; Pinnavaia, T. J. *Science* **1998**, *282*, 1302-1305.
(109) Ung, T.; Liz-Marzan, L. M.; Mulvaney, P. *Langmuir* **1998**, *14*, 3740-3748.
(110) Lu, Y.; McLellan, J.; Xia, Y. *Langmuir* **2004**, *20*, 3464-3470.
(111) Marinakos, S. M.; Novak, J. P.; Brousseau III, L. C.; House, A. B.; Edeki, E. M.; Feldhaus, J. C.; Feldheim, D. L. *J. Am. Chem. Soc.* **1999**, *121*, 8518-8522.
(112) Tissot, I.; Reymond, J. P.; Lefebvre, F.; Bourgeat-Lami, E. *Chem. Mater.* **2002**, *14*, 1325-1331.
(113) Stober, W.; Fink, A.; Bohn, E. *J. Colloid Interface Sci.* **1968**, *26*, 62-69.
(114) Yin, Y.; Lu, Y.; Sun, Y.; Xia, Y. *Nano. Lett.* **2002**, *2*, 427-430.
(115) Donath, E.; Sukhorukov, G. B.; Caruso, F.; Davis, S. A.; Mohwald, H. *Angew. Chem. Int. Ed.* **1998**, *37*, 2202-2205.
(116) Dubas, S. T.; Schlenoff, J. B. *Langmuir* **2001**, *17*, 7725-7727.

(117) Sun, B.; Chiu, D. T. *Anal. Chem.* **2005**, *accepted.*
(118) Chiu, D. T.; Wilson, C. F.; Ryttsen, F.; Stromberg, A.; Farre, C.; Karlsson, A.; Nordholm, S.; Gaggar, A.; Modi, B. P.; Moscho, A.; Garza-Lopez, R. A.; Orwar, O.; Zare, R. N. *Science* **1999**, *283*, 1892-1895.
(119) Eaton, W. A.; Munoz, V.; Stephen J, H.; Jas, G. S.; Lapidus, L. J.; Henry, E. R. *Annu. Rev. Biophys. Biomol. Struct.* **2000**, *29*, 327-359.
(120) Weijer, C. J. *Science* **2003**, *300*, 96-100.
(121) Benkovic, S. J.; Hammes-Schiffer, S. *Science* **2003**, *301*, 1196-1202.
(122) van Oijen, A. M.; Blainey, P. C.; Crampton, D. J.; Richardson, C. C.; Ellenberger, T.; Xie, X. S. *Science* **2003**, *301*, 1235-1238.
(123) Yang, H.; Luo, G.; Karnchanaphanurach, P.; Louie, T.-M.; Rech, I.; Cova, S.; Xun, L.; Xie, X. S. *Science* **2003**, *302*, 262-266.
(124) Strehlow, H. *Rapid Reactions in Solution*; VCH: Weinheim, Federal Republic of Germany, New York, NY, USA, 1992.
(125) Knight, J. B., Vishwanath, A., Brody, J. P., Austin, R. H. *Phys. Rev. Lett.* **1998**, *80*, 3863-3866.
(126) Regenfuss, P.; Clegg, R. M.; Fulwyler, M. J.; Barrantes, F. J.; Jovin, T. M. *Rev. Sci. Inst.* **1985**, *56*, 283-290.
(127) Lipman, E. A.; Schuler, B.; Bakajin, O.; Eaton, W. A. *Science* **2003**, *301*, 1233-1235.
(128) Callender, R.; Dyer, R. B. *Curr. Opin. Struc. Biol.* **2002**, *12*, 628-633.
(129) Crooks, J. E. *J. Phys. E. Sci. Instrum.* **1983**, *16*, 1142-1147.
(130) Kegeles, G. *Methods in Enzymol.* **1978**, *48*, 308-320.
(131) Holten, D.; Windsor, M. W. *Annu. Rev. Biophys. Bioeng.* **1978**, *7*, 189-227.
(132) Plenert, M. L.; Shear, J. B. *Proc. Natl. Acad. Sci., USA* **2003**, *100*, 3853-3857.
(133) Gutman, M. *Methods in Enzymology* **1986**, *127*, 522-538.
(134) Vreeland, W. N.; Locascio, L. *Anal. Chem.* **2003**, *75*, 6906-6911.
(135) Langer, R. *Science* **1990**, *249*, 1527-1533.
(136) Bisby, R. H.; Mead, C.; Morgan, C. G. *FEBS Leters* **1999**, *463*, 165-168.
(137) Bisby, R. H.; Mead, C.; Morgan, C. G. *Photochem Photobiol* **2000**, *72*, 57-61.
(138) Bondurant, B.; Meuller, A.; O'Brien, D. F. *Biochim. Biophys. Acta* **2001**, *1511*, 113-122.
(139) Lamparski, H.; Liman, U.; Barry, J. A.; Ramaswami, V.; Brown, M. F.; O'Brien, D. F. *Biochemistry* **1992**, *31*, 685-694.
(140) Srinivasan, R. *Science* **1986**, *234*, 559-565.
(141) Sjoback, R.; Nygren, J.; Kubista, M. *Spectrochim Acta A* **1995**, *51*, 7.
(142) Klonis, N.; Sawyer, W. H. *J. Fluorescence* **1996**, *6*, 147-157.
(143) Yguerabide, J.; Talavera, E.; Alvarez, J. M.; Quintero, B. *Photochem. Photobiol.* **1994**, *60*, 435-441.
(144) Cheng, Y.-F.; Dovichi, N. J. *Science* **1988**, *242*, 562-564.
(145) Smith, L. M.; Sanders, J. Z.; Kaiser, R. J.; Hughes, P.; Dodd, C.; Connell, C. R.; Heiner, C.; Kent, S. B. H.; Hood, L. E. *Nature* **1986**, *321*, 674-679.
(146) Sjoback, R.; Nygren, J.; Kubista, M. *Spectrochim Acta A* **1995**, *51*, 7.
(147) Jahn, R.; Sudhof, T. C. *Annu. Rev. Biochem.* **1999**, *68*, 863-911.

(148) Berridge, M. J.; Lipp, P.; Bootman, M. D. *Nature reviews, molecular cell biology* **2000**, *1*, 11-21.
(149) Ostberg, B. C.; Sand, O.; Bjoro, T.; Haug, E. *Biotechniques* **2000**, *29*, 1122-1125.
(150) Kao, J. P. Y.; Adams., S. R. *Photosensitive caged compounds: design, properties, and biological applications. In Optical Microscopy: Emerging Methods and Applications.*; Academic Press, London, 1993.
(151) Akaoka, H.; Saunier, C. F.; Chergui, K.; Charlety, P.; Buda, M.; Chouvet, G. *J Neurosci Methods* **1992**, *42*, 119-128.
(152) Angelantonio, S. D.; Nistri, A. *J. Neurosci. Methods* **2001**, *110*, 155-161.
(153) Junginger, H. E. *Adv Drug Deliv Rev* **2002**, *54*, S57-S75.
(154) Awenowicz, P. W.; Porter, L. L. *J. Neurophysiol* **2002**, *88*, 3439-3451.
(155) Hess, G. P.; Grewer, C. *Methods Enzymol.* **1998**, *291*, 443-473.
(156) Hess, G. P. *Archives of Physiology and Biochemistry* **1996**, *104*, 752-761.
(157) Gurney, A. M.; Lester, H. A. *Physiol. Rev.* **1987**, *67*, 583-617.
(158) Adams, S. R.; Tsien, R. Y. *annu. Rev. Physiol.* **1993**, *55*, 755-784.
(159) Denk, W.; Strickler, J. H.; Webb, W. W. *Science* **1990**, *248*, 73-76.
(160) Albota, M.; Beljonne, D.; Brédas, J.-L.; Ehrlich, J. E.; Fu, J.-Y.; Heikal, A. A.; Hess, S. E.; Kogej, T.; Levin, M. D.; Marder, S. R.; McCord-Maughon, D.; Perry, J. W.; Röckel, H.; Rumi, M.; Subramaniam, G.; Webb, W. W.; Wu, X.-L.; Xu, C. *Science* **1998**, *281*, 1653-1656.
(161) Lempert, W. R.; Harris, S. R. *Meas. Sci. Technol.* **2000**, *11*, 1251-1258.
(162) Brown, E. B.; Shear, J. B.; Adams, S. R.; Tsien, R. Y.; Webb, W. W. *Biophys. J.* **1999**, *76*.
(163) Srinivasan, R. *Science* **1986**, *234*, 559-565.
(164) Bisby, R. H.; Mead, C.; Mitchell, A. C.; Morgan, C. G. *BIOCHEMICAL AND BIOPHYSICAL RESEARCH COMMUNICATIONS Lancs, England Univ Salford, Sci Res Inst, Dept Sci Biol, Salford M5 4WT, Lancs, England* **1999**, *262*, 406-410.
(165) Jones, S. V.; Choi, O. H.; Beaven, M. A. *FEBS Lett.* **1991**, *289*, 47-50.
(166) Caulfield, M. P. *Pharmacol. Ther.* **1993**, *58*, 319-379.
(167) Walker, J. W.; McCray, J. A.; Hess, G. P. *Biochemistry* **1986**, *25*, 1799-1805.
(168) Karlsson, R.; Karlsson, A.; Orwar, O. *Journal of Physical Chemistry B* **2003**, *107*, 11201-11207.
(169) Dubertret, B.; Skourides, P.; Norris, D. J.; Noireaux, V.; Brivanlou, A. H.; Libchaber, A. *Science* **2002**, *298*, 1759-1762.
(170) Weijer, C. *Science* **2003**, *300*, 96-100.
(171) Knust, E.; Bossinger, O. *Science* **2002**, *298*, 1955-1959.
(172) Pettit, D. L.; Wang, S. S.-H.; Gee, K. R.; Augustine, G. J. *Neuron* **1997**, *19*, 465-471.
(173) Krause, C. D.; Mei, E.; Xie, J.; Jia, Y.; Bopp, M. A.; Hochstrasser, R. M.; Pestka, S. *Molecular & Cellular Proteomics* **2002**, *1*, 805-815.
(174) Mackenzie, P. J.; Umemiya, M.; Murphy, T. H. *Neuron* **1996**, *16*, 783-795.
(175) Mogami, H.; Nakano, K.; Tepikin, A. V.; Petersen, O. H. *Cell* **1997**, *88*, 49-55.
(176) Edidin, M. *Trends in Cell Biol.* **2001**, *11*, 492-496.
(177) Simons, K.; Ikonen, E. *Nature* **1997**, *387*, 569-572.

(178) Lippincott-Schwartz, J.; Patterson, G. H. *Science* **2003**, *300*, 87-91.
(179) Stephens, D. J.; Allan, V. J. *Science* **2003**, *300*, 82-86.
(180) Denk, W. *Proc. Natl. Acad. Sci. USA* **1994**, *91*, 6629-6633.
(181) McCray, J. A.; Trentham, D. R. *Annu. Rev. Biophys. Biophys. Chem.* **1989**, *18*, 239-270.
(182) Kaplan, J. H.; Somlyo, A. P. *Trends in Neurosciences* **1989**, *12*, 54-59.
(183) Gramham, C. R.; Ellis-Davies; Kaplan, J. H. *Proc. Natl. Acad. Sci. USA* **1994**, *91*, 187-191.
(184) Matijevic, E. *Langmuir* **1994**, *10*, 8-16.
(185) Sun, Y.; Xia, Y. *Science* **2002**, *298*, 2176-2179.
(186) Walde, P.; Ichikawa, S. *Biomolecular Engineering* **2001**, *18*, 143-177.
(187) Nie, S.; Chiu, D. T.; Zare, R. N. *Science* **1994**, *266*, 1018-1021.

Vita

Bingyun Sun

EDUCATION:

03/2005	**Ph. D., Bio-Analytical Chemistry** Department of Chemistry, University of Washington, Seattle, WA
06/2000	**M.S., Biological Chemistry** Department of Chemistry, Fudan University, Shanghai, China
06/1997	**B.S., Chemistry** Department of Chemistry, Fudan University, Shanghai, China

PROFESSIONAL EXPERIENCE:

12/2000-present RESEARCH ASSISTANT, Department of Chemistry, University of Washington, Seattle, WA
Advisor: Professor Daniel T. Chiu

Synthesized liposomes and nanocapsules as drug carriers, constructed optics, developed approaches to study encapsulation efficiency of nanocapsules on single capsule level, created a alternative method of stop-flow to study kinetics of fast reactions, and studied the muscarinic acetylcholine receptor coupled cell-signaling pathway with high spatial and temporal resolution

12/2000-09/2000 TEACHING ASSISTANT, Department of Chemistry, University of Washington, Seattle, WA

09/1997-06/2000 RESEARCH ASSISTANT, Department of Chemistry, Fudan University, Shanghai, China
Advisor: Professor Zhongxian Huang

Constructed and purified cytochrome b_5 (cyt b_5) site-directed mutants, and studied the structure and function relationships of cyt b_5, especially the mutation caused electron transfer rate changes of cyt b_5 with cytochrome c, myoglobin, plastocyanin by stop-flow

06/1997-09/1997 INTERNSHIP, Shanghai Institute of Biochemistry (Chinese Academy of Science), Shanghai, China

Expression and purification of a novel ZNF191 zinc finger protein - ZNF191 protein and its truncated zinc finger region ZNF191 (243-368)

SOCIAL WORK EXPERIENCES:

06/2001-09/2003 CHAIR, Public Relationship Committee, Graduate Student Club, Department of Chemistry, University of Washington, Seattle, WA
Constructed and maintained the club website at http://students.washington.edu/chemgrad/
Promoted and assisted club events, including seminars, parties, socials

06/2001-12/2003 MEMBER, Catalyst Committee, Graduate Student Club, Department of Chemistry, University of Washington, Seattle, WA
Hosted a workshop of "Learning style", speaker: Mr. Jim Borgford-Parnell, Center for Instructional Development and Research, 11/13/03

09/2002-09/2003 CHAIR, Industry Outreach/Liaison Committee, Nanotechnology Association, Center of Nanotechnology, University of Washington, Seattle, WA
Hosted a seminar of "Salary negotiation", speaker: Ms. Heather Malcolm, Seattle Genetics, 04/11/03

AWARDS AND HONORS:

2001-2003	UIF Nanotechnology Fellowship at University of Washington
2002-2003	Berkelhammer Award at Department of Chemistry, University of Washington
1997-2000	University Graduate Student Grant at Fudan University
1993-1997	The second or third class scholarship at Fudan University
1993	Championship of National Chemistry Olympiad, Shangxi Province, China

PRESENTATIONS:

03/13/2005 **ACS National Conference Presentation (oral):**
"Spatially and Temporally Resolved Delivery of Stimuli onto Single Cells" **Sun, B.** and Chiu, D. T., University of Washington, *ACS 229th national meeting*, San Diego

08/04/2003 **SPIE International Conference Presentation (oral):**
"Cell Signaling Studies with Controlled Stimulation Using Micro/Nano-Capsules and Laser Manipulation", **Sun, B.** and Chiu, D. T., University of Washington, *SPIE International Symposium, 48th Annual meeting*, San Diego

04/22/2003 **Seminar Presentation (oral):**
"Spatially and Temporally Resolved Delivery of Stimuli onto Single Cells", **Sun, B.** and Chiu, D. T., *Nanotechnology Seminar Series*, University of Washington

10/22/2002 **Hosted Presentation:**
"Nanopore Technology: Prospects for Haplotyping and High-Speed Single Molecule DNA Sequencing", Higgins Research Professor of Biology at Harvard University Branton, D., *Nanotechnology Seminar Series*, University of Washington

PUBLICATIONS

(1) **Sun, B.**; Mutch, S.; Lorenz, R.; Chiu, D. T., "Layered polyelectrolyte-silica coating for nanocapsules", *J. Am. Chem. Soc.*, **2005**, *submitted.*
(2) **Sun, B.** and Chiu, D. T., "Determination of the Encapsulation Efficiency of Individual Vesicles Using Single-Vesicle Photolysis and Confocal Single-Molecule Detection". *Anal. Chem.*, **2005**, *accepted.*
(3) **Sun, B.**; Lim, S. D.; Kuo, J. S.; Kuyper, C. L.; Chiu, D. T., "Fast Initiation of Chemical Reactions with Laser-Induced Breakdown of a Nanoscale Partition", *Langmuir*, **2004**, *20,* 9437-9440.
(4) **Sun, B.**; and Chiu, D. T., "Synthesis, Loading, and Application of Individual Nanocapsules for Probing Single-Cell Signaling", *Langmuir*, **2004**, *20*, 4614-4620.
(5) **Sun, B.**; and Chiu, D. T., "Spatially and Temporally Resolved Delivery of Stimuli to Single Cells", *J. Am. Chem. Soc.* **2003**, *125*, 3702-3703.
(6) **Sun, B.**; and Chiu, D. T. "Functional mapping of cell surface proteins with localized stimulation of single cells", *The Proceedings of SPIE*, **2003**, 5222 (Nanocrystals and Organic and Hybrid Nanomaterials), 118-125.
(7) Yao, P.; Wang, Y. H.; **Sun, B.**; Xie, Y.; Hirota, S.; Yamauchi, O.; Huang, Z. X. "Kinetic studies on the oxidation of cytochrome b(5) Phe35 mutants with cytochrome c, plastocyanin and inorganic complexes", *J. Biol. Inorg. Chem.* **2002**, *7*, 375-383.
(8) Yao, P.; Wu, H.; Wang, Y. H.; **Sun, B.**; Xia, Z. X.; Huang, Z. X. "X-ray crystallography, CD and kinetic studies revealed the essence of the abnormal behaviors of the cytochrome b(5) Phe35-> Tyr mutant" *Eur. J. Biochem.* **2002**, *269*, 4287-4296.

(9) Wu, J.; Wang, Y. H.; Gan, J. H.; Wang, W. H.; **Sun, B.** Y.; Huang, Z. X.; Xia, Z. X. "Structures of cytochrome b(5) mutated at the charged surface- residues and their interactions with cytochrome c" *Chinese Journal of Chemistry* **2002**, *20*, 1225-1234.

(10) Huang, Z. X.; **Sun, B.**; Wang, Y. H.; Wang, W. H.; Yao, P.; Xie, Y. "Electrostatic effect on electron transfer between cytochrome b(5) and cytochrome c", *Prog. Nat. Sci.* **2000**, *10*, 393-397.

(11) Sun, Y. L.; Wang, Y. H.; Yan, M. M.; **Sun, B.**; Xie, Y.; Huang, Z. X.; Jiang, S. K.; Wu, H. M. "Structure, interaction and electron transfer between cytochrome b(5), its E44A and/or E56A mutants and cytochrome c", *J. Mol. Biol.* **1999**, *285*, 347-359.

(12) Liu, Y. Q.; Yu, L.; Yu, W. H.; Shi, S. L.; **Sun, B.**; Wu, G. J.; Huang, Z. X. "Expression and purification of a novel ZNF191 zinc finger protein - ZNF191 protein and its truncated zinc finger region ZNF191 (243-368)", *Sci. China Ser. B-Chem.* **1999**, *42*, 245-252

PATENT:

(1) Chiu, D. T., **Sun, B.**, Shelby, P. J., Edgar, J. S., Jeffries, G., Lorenz, R. M., Kuo, J. S., He, M., Allen, P. B., Mutch, S., Kuyper, C. L., Fiorini, G., Lim, D. S. W., "Integrated platform for chemical profiling of ultrasmall subcellular compartments from a single cell", **2004,** US patent application No. 10/926,656.